Geosci. Model Dev., 5, 369–411, 2012
www.geosci-model-dev.net/5/369/2012/
doi:10.5194/gmd-5-369-2012

Geoscientific Model Development

CAM-chem: description and evaluation of interactive atmospheric chemistry in the Community Earth System Model

J.-F. Lamarque[1], L. K. Emmons[1], P. G. Hess[2], D. E. Kinnison[1], S. Tilmes[1], F. Vitt[1], C. L. Heald[3], E. A. Holland[1], P. H. Lauritzen[1], J. Neu[4], J. J. Orlando[1], P. J. Rasch[5], and G. K. Tyndall[1]

[1]National Center for Atmospheric Research, Boulder, CO, USA
[2]Cornell University, Ithaca, NY, USA
[3]Colorado State University, Fort Collins, CO, USA
[4]Jet Propulsion Laboratory, Pasadena, CA, USA
[5]Pacific Northwest National Laboratory, Richland, WA, USA

Correspondence to: J.-F. Lamarque (lamar@ucar.edu)

Received: 8 August 2011 – Published in Geosci. Model Dev. Discuss.: 16 September 2011
Revised: 24 February 2012 – Accepted: 6 March 2012 – Published: 27 March 2012

Abstract. We discuss and evaluate the representation of atmospheric chemistry in the global Community Atmosphere Model (CAM) version 4, the atmospheric component of the Community Earth System Model (CESM). We present a variety of configurations for the representation of tropospheric and stratospheric chemistry, wet removal, and online and offline meteorology. Results from simulations illustrating these configurations are compared with surface, aircraft and satellite observations. Major biases include a negative bias in the high-latitude CO distribution, a positive bias in upper-tropospheric/lower-stratospheric ozone, and a positive bias in summertime surface ozone (over the United States and Europe). The tropospheric net chemical ozone production varies significantly between configurations, partly related to variations in stratosphere-troposphere exchange. Aerosol optical depth tends to be underestimated over most regions, while comparison with aerosol surface measurements over the United States indicate reasonable results for sulfate , especially in the online simulation. Other aerosol species exhibit significant biases. Overall, the model-data comparison indicates that the offline simulation driven by GEOS5 meteorological analyses provides the best simulation, possibly due in part to the increased vertical resolution (52 levels instead of 26 for online dynamics). The CAM-chem code as described in this paper, along with all the necessary datasets needed to perform the simulations described here, are available for download at www.cesm.ucar.edu.

1 Introduction

Atmospheric chemistry plays an integral role in the distribution of the non-CO_2 radiatively active gases and aerosols (Forster et al., 2007). In addition, climate and its evolution strongly influences atmospheric chemistry and air quality (Chen et al., 2009; Jacob and Winner, 2009). Because of the nonlinear behavior of chemistry and the importance of regionally-varying emissions, it is critical to represent the interactions between chemistry and climate using a global three-dimensional model.

We discuss here the representation of atmospheric chemistry (gas phase and aerosol species) in the global Community Atmosphere Model (CAM version 4, Neale et al., 2011), the atmospheric component of the Community Earth System Model (CESM). Due to its full integration in the CESM, CAM-chem provides the flexibility of using the same code to perform climate simulations and simulations with specified meteorological fields. Therefore, CAM-chem can be used in three separate modes, all embedded within CESM: (1) a fully coupled Earth System model (i.e., with all climate components active, which offers the possibility to connect the chemistry with biogeochemical processes in the land and ocean models), (2) with specified sea-surface and sea-ice distributions and (3) with specified meteorological fields. Configurations (1) and (2) are usually referred to as online, while configuration (3) is referred to as offline. In configurations (2) and (3), only the atmosphere and land components of CESM are active. When run in a fully coupled mode, the ocean and ice dynamics are also allowed to respond to

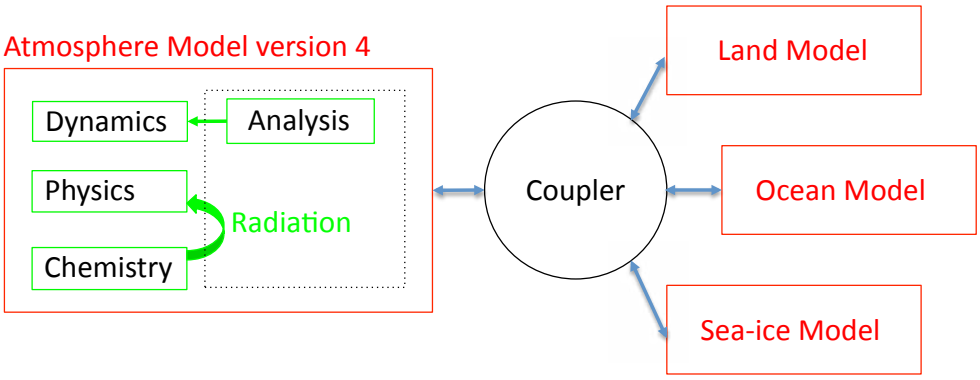

Fig. 1. Schematic representation of the Community Earth System Model. The dotted box indicates the features associated with the use of specified dynamics (use of meteorological analyses and lack of feedback through radiation).

changes in the atmosphere. This allows "slow responses" (for example in ocean currents and ice extent) within the climate system to occur that are prevented in modes 2 and 3. Mode 2 only allows fast atmospheric responses, and land responses to occur, while mode 3 does not allow any meteorological responses.

The availability of a specified dynamics configuration of CAM-chem offers a number of advantages over traditional chemistry-transport models. (1) It allows for consistent simulations between the online and offline versions; (2) it allows the offline version to be run in an Earth System framework so as to fully exploit other model components. In particular it allows an incorporation of the biogeochemical algorithms in the land components; (3) it allows for the radiative algorithms incorporated into CAM4 to be fully exploited in the offline version. This allows a calculation of the instantaneous radiative forcing within the offline model version, including a calculation of the instantaneous radiative forcing for specific events (e.g., forest fires) (Pfister et al., 2008; Randerson et al., 2006); (4) it allows for the strict conservation of tracer mass by accounting for changes in mixing ratio as the water vapor concentration changes within the atmosphere. In addition, CAM-chem uses a chemical preprocessor that provides extensive flexibility in the definition of the chemical mechanism, allowing for ease of update and modification.

Recent applications of CAM-chem have demonstrated its ability to represent tropospheric (Aghedo et al., 2011; Lamarque et al., 2010, 2011a, b) and stratospheric (Lamarque et al., 2008; Lamarque and Solomon, 2010) conditions, including temperature structure and dynamics (Butchart et al., 2011). Offline CAM-chem has been used in the Hemispheric Transport of Air Pollution (HTAP) assessments (Anenberg et al., 2009; Fiore et al., 2009; Jonson et al., 2010; Shindell et al., 2008; Sanderson et al., 2008).

It is the purpose of this paper to document all these aspects of CAM-chem, along with results from associated simulations and their evaluation against observations. The paper is therefore organized as follows: in Sect. 2, we provide a short introduction to CAM4. In Sect. 3, we discuss all the chemistry-specific parameterizations of CAM-chem. The implementation of the specified-dynamics version is discussed in Sect. 4. Section 5 presents the various chemical mechanisms used in this study. Model simulation setups, including emissions are discussed in Sect. 6, while the comparison to observations is shown in Sect. 7. Discussion and conclusions are in Sect. 8.

2 CAM4 description and definition of CAM-chem

CAM-chem refers to the implementation of atmospheric chemistry in the Community Earth System Model (CESM). All the subroutines responsible for the representation of chemistry are included in the build of CESM only when explicitly requested; therefore a user only interested in a climate simulation (for which the atmospheric composition is specified) is not impacted by the additional code and additional cost to simulate chemistry. The chemistry is fully integrated into the Community Atmosphere Model (Fig. 1), meaning that the representation of dynamics (including transport) and physics (radiation, convection and large-scale precipitation, boundary-layer and diffusion) is the same whether the model is using computed (online) or specified (specified dynamics, dotted box in Fig. 1) meteorological fields. CAM-chem is therefore CAM4 with chemistry activated.

In the configurations described in this paper, atmospheric chemistry interacts with the climate only through radiation since no cloud-aerosol interaction is available in CAM4; the impact on temperature is of course overwritten in the case of specified dynamics. Also, the ocean and sea-ice components of the CESM are inactive due to the use of specified sea-surface temperatures and sea-ice distribution. On the other hand, the land component is fully active and provides the chemistry with deposition velocities and biogenic emissions.

Table 1. Plant functional types in land model of the CESM.

Index	Plant functional type
1	desert, ice and ocean
2	needleleaf evergreen temperate tree
3	needleleaf evergreen boreal tree
4	needleleaf deciduous temperate tree
5	broadleaf evergreen tropical tree
6	broadleaf evergreen temperate tree
7	broadleaf deciduous tropical tree
8	broadleaf deciduous temperate tree
9	broadleaf deciduous boreal tree
10	broadleaf evergreen shrub
11	broadleaf deciduous temperate shrub
12	broadleaf deciduous boreal shrub
13	C_3 arctic grass
14	C_3 non-arctic grass
15	C_4 grass
16	corn
17	wheat

When CAM4 is run without chemistry, it uses prescribed ozone and aerosol fields, usually monthly-averaged three-dimensional fields from a previously performed simulation with CAM-chem.

The Community Atmosphere Model, version 4 (CAM4, Neale et al., 2011) was released as the atmosphere component of the Community Climate System Model, version 4 (CCSM4) and contains improvements over CAM3 (Collins et al., 2006). In particular, the finite volume dynamical core option available in CAM3 is now the default primarily due to its superior tracer transport properties (Rasch et al., 2006). As in CAM3, deep convection is parameterized using the Zhang-McFarlane approach (1995), but with modifications as discussed below, while shallow convection follows Hack et al. (2006). Additional information on the representation of clouds and precipitation processes can be found in Boville et al. (2006). Finally, processes in the planetary boundary layer are represented using the Holtslag and Boville (1993) parameterization. The vertical coordinate is a hybrid sigma-pressure.

Changes made to the representation of deep convection include a dilute plume calculation and the introduction of Convective Momentum Transport (CMT; Richter and Rasch, 2007; Neale et al., 2008). In addition, the cloud fraction has an additional calculation to improve thermodynamic consistency. A freeze-drying modification is further made to the cloud fraction calculation in very dry environments, such as Arctic winter, where cloud fraction and cloud water estimates were somewhat inconsistent in CAM3.

Altogether, only marginal improvements over CAM3 are found in the large-scale aspects of the simulated climate (see Neale et al., 2011 for a complete description of the model performance). Indeed, it is found that the implementation of the finite volume dynamical core leads to a degradation in the excessive trade-wind simulation, but with an accompanying reduction in zonal stresses at higher latitudes. But, CMT reduces much of the excessive trade-wind biases. Plume dilution leads to moister deep tropics alleviating much of the mid-tropospheric dry biases and reduces the persistent precipitation biases over the Arabian peninsula and the southern Indian ocean associated with the Indian Monsoon. Finally, the freeze-drying modification alleviates much of the wintertime excessive cloud bias and improves the associated surface cloud-related energy budget.

3 Chemistry-specific parameterizations

CAM-chem borrows heavily from MOZART-4 (Emmons et al., 2010, referenced hereafter as E2010). In particular, many of the parameterizations needed to represent atmospheric chemistry in a global model are adapted or expanded from their equivalents in MOZART-4. However, for completeness, we will include a brief description of those parameterizations (and their updates, whenever applicable).

3.1 Dry deposition

Dry deposition is represented following the resistance approach originally described in Wesely (1989); as discussed in E2010, this earlier paper was subsequently updated and we have included all updates (Walcek et al., 1986; Walmsley and Wesely, 1996; Wesely and Hicks, 2000). Following this approach, all deposited chemical species (the specific list of deposited species is defined along with the chemical mechanisms, see Sect. 4) are mapped to a weighted-combination of ozone and sulfur dioxide depositions; this combination represents a definition of the ability of each considered species to oxidize or to be taken up by water. In particular, the latter is dependent on the effective Henry's law coefficient. While this weighting is applicable to many species, we have included specific representations for CO/H_2 (Yonemura et al., 2000; Sanderson et al., 2003), and peroxyacetylnitrate (PAN, Sparks et al., 2003; Turnipseed et al., 2006). Furthermore, it is assumed that the surface resistance for SO_2 can be neglected (Walcek et al., 1986). Finally, following Cooke et al. (1999), the deposition velocities of black and organic carbonaceous aerosols are specified to be $0.1\,\mathrm{cm\,s^{-1}}$ over all surfaces. Dust and sea-salt are represented following Mahowald et al. (2006a, b).

The computation of deposition velocities in CAM-chem takes advantage of its coupling to the Community Land Model (CLM; Oleson et al., 2010, also see http://www.cesm.ucar.edu/models/cesm1.0/clm/CLM4_Tech_Note.pdf). In particular, the computation of surface resistances in CLM leads to a representation at the level of each plant functional type (Table 1) of the various drivers for deposition velocities. The grid-averaged velocity is computed as the

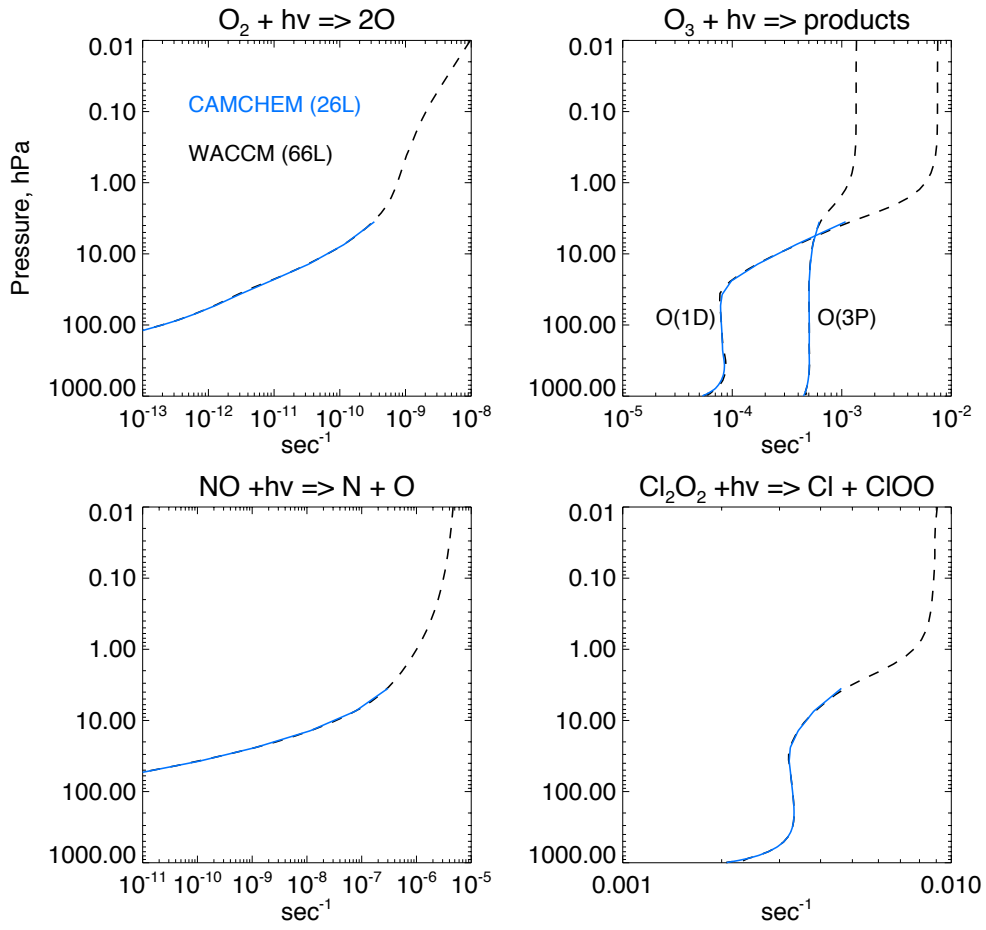

Fig. 2. Photolysis rates in CAM and WACCM for 1 January, noon at 0° N conditions.

weighted-mean over all land cover types available at each grid box. This ensures that the impact on deposition velocities from changes in land cover, land use or climate can be taken into account.

In addition, the same dry deposition approach is separately applied to water surfaces i.e., lakes and oceans, including sea-ice. It is then combined with the land-based value, weighted by the ocean/sea-ice and land fractions in each model grid cell.

3.2 Biogenic emissions

Similar to the treatment of dry deposition over land, biogenic emissions of volatile organic compounds (isoprene and monoterpenes) are calculated based upon the land cover. These are made available for atmospheric chemistry, unless the user decides to explicitly set those emissions using predefined (i.e., contained in a file) gridded values. Details of this implementation in the CLM3 are discussed in Heald et al. (2008); we provide a brief overview here.

Vegetation in the CLM model is described by 17 plant function types (PFTs, see Table 1). Present-day land surface parameters such as leaf area index are consistent with MODIS land surface data sets (Lawrence and Chase, 2007). Alternate land cover and density can be either specified or interactively simulated with the dynamic vegetation model of the CLM for any time period of interest.

Isoprene emissions follow the MEGAN2 (Guenther et al., 2006) algorithms for a detailed canopy model (CLM). This includes mapped PFT-specific emission factors to account for species divergent emissions of isoprene. These standard emission factors are modulated by activity factors accounting for the effect of temperature, radiation, leaf age, vegetation density (identified by the leaf-area index) and soil moisture. The annual totals are in the range of 500–600 Tg yr^{-1}, depending on model configuration and associated climate conditions (see Table 9).

Total monoterpene emissions follow the earlier work of Guenther et al. (1995) as implemented in the CLM by Levis et al. (2003). Baseline emission factors are specified for each plant function type and are scaled by an exponential function of leaf temperature.

Table 2. List of input fields required for specified dynamics in CAM.

Variable	Physical description (units, geometric dimensions)
U	zonal wind component ($m\,s^{-1}$, 3-D)
V	meridional wind component ($m\,s^{-1}$, 3-D)
T	temperature (K, 3-D)
PS	surface pressure (Pa, 2-D)
PHIS	surface geopotential ($m^2\,s^{-2}$, 2-D)
TS	surface temperature (K, 2-D)
TAUX	zonal surface stress ($N\,m^{-2}$, 2-D)
TAUY	meridional surface stress ($N\,m^{-2}$, 2-D)
SHFLX	sensible heat flux ($W\,m^{-2}$, 2-D)
LHFLX	latent heat flux ($W\,m^{-2}$, 2-D), computed from moisture flux
OCNFRAC	Grid cell fraction over ocean used in dry deposition (2-D)
ICEFRAC	Grid cell fraction over ocean ice used in dry deposition, based on meteorology surface temperatures (2-D)

3.3 Wet deposition

Wet removal of soluble gas-phase species is the combination of two processes: in-cloud, or nucleation scavenging (rainout), which is the local uptake of soluble gases and aerosols by the formation of initial cloud droplets and their conversion to precipitation, and below-cloud, or impaction scavenging (washout), which is the collection of soluble species from the interstitial air by falling droplets or from the liquid phase via accretion processes (e.g., Rotstayn and Lohmann, 2002). Removal is modeled as a simple first-order loss process $X_{\text{iscav}}=X_i \times F \times (1-\exp(-\lambda\ \Delta t))$. In this formula, X_{iscav} is the species mass (in kg) of X_i scavenged in time step Δt, F is the fraction of the grid box from which tracer is being removed, and λ is the loss rate. In-cloud scavenging is proportional to the amount of condensate converted to precipitation, and the loss rate depends on the amount of cloud water, the rate of precipitation formation, and the rate of tracer uptake by the liquid phase. Below-cloud scavenging is proportional to the precipitation flux in each layer and the loss rate depends on the precipitation rate and either the rate of tracer uptake by the liquid phase (for accretion processes), the mass-transfer rate (for highly soluble gases and small aerosols), or the collision rate (for larger aerosols). In CAM-chem two separate parameterizations are available: Horowitz et al. (2003) from MOZART-2 and Neu and Prather (2011).

The distinguishing features of the Neu and Prather scheme are related to three aspects of the parameterization: (1) the partitioning between in-cloud and below cloud scavenging, (2) the treatment of soluble gas uptake by ice and (3) accounting for the spatial distribution of clouds in a column and the overlap of condensate and precipitation. Given a cloud fraction and precipitation rate in each layer, the scheme determines the fraction of the gridbox exposed to precipitation from above and that exposed to new precipitation formation under the assumption of maximum overlap of the precipitating fraction. Each model level is partitioned into as many as four sections, each with a gridbox fraction, precipitation rate, and precipitation diameter: (1) cloudy with precipitation falling through from above; (2) cloudy with no precipitation falling through from above; (3) clear sky with precipitation falling through from above; (4) clear sky with no precipitation falling from above. Any new precipitation formation is spread evenly between the cloudy fractions (1 and 2). In region 3, we assume a constant rate of evaporation that reduces both the precipitation area and amount so that the rain rate remains constant. Between levels, we average the properties of the precipitation and retain only two categories, precipitation falling into cloud and precipitation falling into ambient air, at the top boundary of each level. If the precipitation rate drops to zero, we assume full evaporation and random overlap with any precipitating levels below. Our partitioning of each level and overlap assumptions are in many ways similar to those used for the moist physics in the ECMWF model (Jakob and Klein, 2000).

The transfer of soluble gases into liquid condensate is calculated using Henry's Law, assuming equilibrium between the gas and liquid phase. Nucleation scavenging by ice, however, is treated as a burial process in which trace gas species deposit on the surface along with water vapor and are buried as the ice crystal grows. Kärcher and Voigt (2006) have found that the burial model successfully reproduces the molar ratio of HNO_3 to H_2O on ice crystals as a function of temperature for a large number of aircraft campaigns spanning a wide variety of meteorological conditions. We use the empirical relationship between the HNO_3:H_2O molar ratio and temperature given by Kärcher and Voigt (2006) to determine in-cloud scavenging during ice particle formation, which is applied to nitric acid only. Below-cloud scavenging by ice is calculated using a rough representation of the riming process modeled as a collision-limited first order loss process. Neu and Prather (2011) provide a full description of the scavenging algorithm.

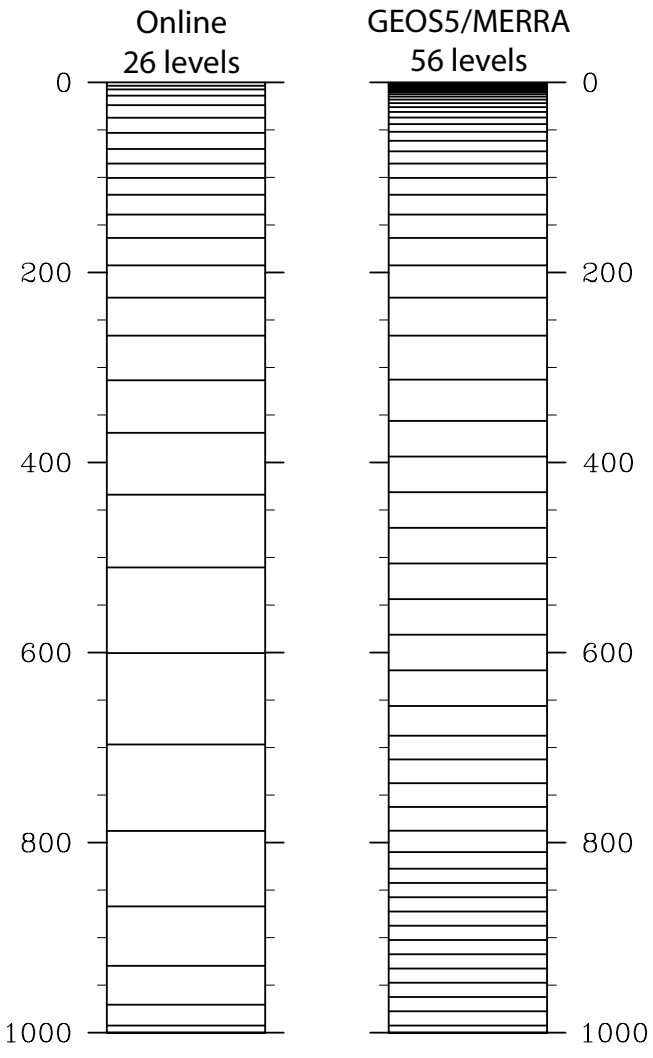

Fig. 3. Distribution of vertical levels in the various model configurations.

On the other hand, the Horowitz approach uses the rain generation diagnostics from the large-scale and convection precipitation parameterizations in CAM; equilibrium between gas-phase and liquid phase is then assumed based on the effective Henry's law. Below-cloud removal is applied to nitric acid and hydrogen peroxide only.

While using the same information on rain formation and precipitation, the wet removal of aerosols is handled separately, using the parameterization described in Barth et al. (2000).

3.4 Lightning

The emissions of NO from lightning are included as in E2010, i.e., using the Price parameterization (Price and Rind, 1992; Price et al., 1997), scaled to provide a global annual emission of 3–5 Tg(N) yr^{-1} (see Table 9), slightly lower than the global estimate of Hudman et al. (2007). This range is due to interannnual variability in convective activity. The vertical distribution follows DeCaria et al. (2006) as in E2010. In addition, the strength of intra-cloud (IC) lightning strikes is assumed to be equal to cloud-to-ground strikes, as recommended by Ridley et al. (2005).

3.5 Polar stratospheric clouds and associated ozone depletion

The representation of polar stratospheric clouds is an update over the version used in all the CCMval-2 analysis papers (e.g., Austin et al., 2010) in which it was shown that CAM-chem (identified in those studies as CAM3.5) was underestimating the extent and depth of Antarctic ozone hole depletion. In particular, we are now using a strict enforcement of the conservation of total (organic and inorganic) chlorine and total bromine under advection. Indeed, it has been identified that the existence of strong gradients in the stratosphere led to non-conservation issues of the total bromine and chlorine, as computed from the sum of their components, related to inaccuracies in transport algorithms. We are therefore forcing the conservation through the addition of two additional tracers: TCly and TBry. These tracers are specified at the lower boundary and reflect the total amount of Br and Cl atoms (organic and inorganic) in the atmosphere following the observed concentrations of all considered halogen species in the model. To ensure mass conservation, at each grid point the total mass after advection of the summed Cl-containing species is scaled to be the same as the mass of TCly. Uniform scaling is applied to each component. The overall impact is to increase the amount of reactive bromine and chlorine in the polar stratosphere and, consequently, of ozone loss.

In addition, we have updated the heterogeneous chemistry module to reflect that the model was underestimating the supercooled ternary solution (STS) surface area density (SAD). Heterogeneous processes on liquid sulfate aerosols and polar stratospheric clouds are included following the approach of Considine et al. (2000). This approach represents the surface area density, effective radius, and composition of liquid binary sulfate (LBS), supercooled ternary solution (STS), nitric acid tri-hydrate (NAT), and water-ice. There are six heterogeneous reactions on liquid sulfate aerosol (LBS or STS), five reactions on solid NAT aerosol, and six reactions on solid water-ice aerosol. The process of denitrification is derived in the chemistry module; the process of dehydration is derived in the prognostic H_2O approach used in CAM. Details of the heterogeneous module are discussed in Kinnison et al., 2007. This previous version (used in the CCMval-2 simulations) allowed the available HNO_3 to first form nitric acid trihydrate (NAT); then the resulting gas-phase HNO_3 was available to form STS SAD. In the new version the approach is reversed, with the available HNO_3 to first form STS aerosol. This enhances the STS SAD that is used to derive heterogeneous conversion of reservoir species to more active, odd-oxygen

Table 3. List of species in the considered chemical mechanisms. In addition, we list the chemical solver (Explicit or Implicit), the potential use of emissions of lower-boundary conditions and of deposition processes (wet and dry).

Number	Species name*	Formula	Solver	Emissions	Boundary condition	Wet deposition	Dry deposition
1	ALKO2	$C_5H_{11}O_2$	I				
2	ALKOOH	$C_5H_{12}O_2$	I			X	X
3	BIGALD	$C_5H_6O_2$	I	X			
4	BIGALK	C_5H_{12}	I	X			
5	BIGENE	C_4H_8	I	X			
6	C10H16		I	X			
7	C2H2		I	X			
8	C2H4		I	X			
9	C2H5O2		I				
0	C2H5OH		I	X		X	X
11	C2H5OOH		I			X	X
12	C2H6		I	X			
13	C3H6		I	X			
14	C3H7O2		I				
15	C3H7OOH		I			X	
16	C3H8		I	X			
17	CH2O		I	X		X	X
18	CH3CHO		I	X		X	X
19	CH3CN		I	X		X	X
20	CH3CO3		I				
21	CH3COCH3		I	X			X
22	CH3COCHO		I				X
23	CH3COOH		I	X		X	X
24	CH3COOOH		I			X	X
25	CH3O2		I				
26	CH3OH		I	X		X	X
27	CH3OOH		I			X	
28	CH4		E		X		
29	CO		E	X			X
30	CRESOL	C_7H_8O	I				
31	DMS	CH_3SCH_3	I	X			
32	ENEO2	$C_4H_9O_3$	I				
33	EO	$HOCH_2CH_2O$	I				
34	EO2	$HOCH_2CH_2O_2$	I				
35	GLYALD	$HOCH_2CHO$	I			X	X
36	GLYOXAL	$C_2H_2O_2$	I				
37	H2		E		X		
38	H2O2		I			X	X
39	HCN		I	X		X	X
40	HCOOH		I	X		X	X
41	HNO3		I			X	X
42	HO2		I				
43	HOCH2OO		I				
44	HO2NO2		I			X	X
45	HYAC	CH_3COCH_2OH	I			X	X
46	HYDRALD	$HOCH_2CCH_3CHCHO$	I			X	X
47	ISOP	C_5H_8	I	X			
48	ISOPNO3	$CH_2CHCCH_3OOCH_2ONO_2$	I			X	
49	ISOPO2	$HOCH_2COOCH_3CHCH_2$	I				
50	ISOPOOH	$HOCH_2COOHCH_3CHCH_2$	I			X	X

* The convention in the "Species name" column refers to the actual naming as it appears in the code (limited to 8 characters). All chemistry subroutines can identify the array index for a specific species through query functions associated with the name as listed here.

Table 3. Continued.

Number	Species name	Formula	Solver	Emissions	Boundary condition	Wet deposition	Dry deposition
51	MACR	CH_2CCH_3CHO	I			X	
52	MACRO2	$CH_3COCHO_2CH_2OH$	I				
53	MACROOH	$CH_3COCHOOHCH_2OH$	I			X	X
54	MCO3	$CH_2CCH_3CO_3$	I				
55	MEK	C_4H_8O	I	X			
56	MEKO2	$C_4H_7O_3$	I				
57	MEKOOH	$C_4H_8O_3$	I			X	X
58	MPAN	$CH_2CCH_3CO_3NO_2$	I				X
59	MVK	$CH_2CHCOCH_3$	I			X	
60	N2O		E		X		
61	N2O5		I				
62	NH3		I	X		X	X
63	NO		I	X			X
64	NO2		I	X			X
65	NO3		I				
66	O		I				
67	O1D	O	I				
68	O3		I				X
69	OH		I				
70	ONIT	$CH_3COCH_2ONO_2$	I			X	X
71	ONITR	$CH_2CCH_3CHONO_2CH_2OH$	I			X	X
72	Pb		E				X
73	PAN	$CH_3CO_3NO_2$	I				X
74	PO2	$C_3H_6OHO_2$	I				
75	POOH	C_3H_6OHOOH	I			X	X
76	Rn		E	X			
77	RO2	$CH_3COCH_2O_2$	I				
78	ROOH	CH_3COCH_2OOH	I			X	X
79	SO2		I	X		X	X
80	TERPO2	$C_{10}H_{17}O_3$	I				
81	TERPOOH	$C_{10}H18O_3$	I			X	X
82	TOLO2	$C_7H_9O_5$	I				
83	TOLOOH	$C_7H_{10}O_5$	I			X	X
84	TOLUENE	C_7H_8	I	X			
85	XO2	$HOCH_2COOCH_3CHOHCHO$	I				
86	XOH	$C_7H_{10}O_6$	I				
87	XOOH	$HOCH_2COOHCH_3CHOHCHO$	I			X	X
	Bulk aerosol species						
1	CB1	C, hydrophobic black carbon	I	X			X
2	CB2	C, hydrophilic black carbon	I	X		X	X
3	DST01	$AlSiO_5$	I	X		X	X
4	DST02	$AlSiO_5$	I	X		X	X
5	DST03	$AlSiO_5$	I	X		X	X
6	DST04	$AlSiO_5$	I	X		X	X
7	NH4		I			X	X
8	NH4NO3		I			X	X
9	OC1	C, hydrophobic organic carbon	I	X			X
10	OC2	C, hydrophilic organic carbon	I	X		X	X
11	SOA	C_{12}	I			X	X
12	SO4		I	X		X	X
13	SSLT01	NaCl	I	X		X	X
14	SSLT02	NaCl	I	X		X	X
15	SSLT03	NaCl	I	X		X	X
16	SSLT04	NaCl	I	X		X	X

Table 3. Continued.

Number	Species name	Formula	Solver	Emissions	Boundary condition	Wet deposition	Dry deposition
	Stratospheric species						
1	BRCL	BrCl	I				
2	BR	Br	I				
3	BRO	BrO	I				
4	BRONO2	$BrONO_2$	I			X	
5	BRY		E		X		
6	CCL4	CCl_4	E		X		
7	CF2CLBR	CF_2ClBr	E		X		
8	CF3BR	CF_3Br	E		X		
9	CFC11	$CFCl_3$	E		X		
10	CFC12	CF_2Cl_2	E		X		
11	CFC13	CCl_2FCClF_2	E		X		
12	CH3CL	CH_3Cl	E		X		
13	CH3BR	CH_3Br	E		X		
14	CH3CCL3	CH_3CCl_3	E		X		
15	CLY		E		X		
16	CL	Cl	I				
17	CL2	Cl_2	I				
18	CLO	ClO	I				
19	CLONO2	$ClONO_2$	I			X	
20	CO2		E		X		
21	OCLO	OClO	I				
22	CL2O2	Cl_2O_2	I				
23	H		I				
24	H2O		I	X			
25	HBR	HBr	I			X	
26	HCFC22	CHF_2Cl	E		X		
27	HCL	HCl	I			X	
28	HOBR	HOBr	I			X	
29	HOCL	HOCl	I			X	
30	N		I				

depleting species. Observational studies have shown that STS is the main PSC for odd-oxygen loss and therefore this is a better representation of stratospheric heterogeneous processes (e.g., Lowe and MacKenzie, 2008). After formation of STS aerosol, there is still enough gas-phase HNO_3 available to form NAT. The effective radius of NAT is then used to settle the condensed phase HNO_3 and eventual irreversible denitrification occurs. These updates have led to a considerable improvement in the representation of the polar stratospheric ozone loss (see Sect. 7.4).

3.6 Photolysis

In CAM-chem, for wavelengths longer than 200 nm (up to 750 nm), the lookup table approach from MOZART-3 (Kinnison et al., 2007) is the only method available at this time. We have also included the online calculation of photolysis rates for wavelengths shorter than 200 nm (121–200 nm) from MOZART-3; this was shown to be important for ozone chemistry in the tropical upper troposphere (Prather, 2009). Therefore, the combined (online-lookup table) approach is used in all model configurations. In addition, because the standard configuration of CAM only extends into the lower stratosphere (model top is $\approx$ 40 km), we have included an additional layer of ozone and oxygen above the model top to provide a very accurate representation of photolysis rates in the upper portion of the model (Fig. 2) as compared to the equivalent calculation using a fully-resolved stratospheric distribution. The fully resolved stratospheric module was evaluated in Chapter 6 of the SPARC CCMVal report on the Evaluation of Chemistry-Climate Models. This photolysis module was shown to be one of the more accurate modules used in CCMs (see SPARC, 2010 for details).

Table 4. List of reactions. Temperature (T) is expressed in K, pressure (P) in Pa, air density (M) in molec cm^{-3}, ki and ko in cm^3 molec^{-1} s^{-1}.

Tropospheric photolysis	Rate
O2 +*hv* → 2*O	
O3 +*hv* → O1D + O2	
O3 +*hv* → O + O2	
N2O +*hv* → O1D + N2	
NO +*hv* → N + O	
NO2 +*hv* → NO + O	
N2O5 +*hv* → NO2 + NO3	
N2O5 +*hv* → NO + O + NO3	
HNO3 +*hv* → NO2 + OH	
NO3 +*hv* → NO2 + O	
NO3 +*hv* → NO + O2	
HO2NO2 +*hv* → OH + NO3	
HO2NO2 +*hv* → NO2 + HO2	
CH3OOH +*hv* → CH2O + H + OH	
CH2O +*hv* → CO + 2*H	
CH2O +*hv* → CO + H2	
H2O2 +*hv* → 2*OH	
CH3CHO +*hv* → CH3O2 + CO + HO2	
POOH +*hv* → CH3CHO + CH2O + HO2 + OH	
CH3COOOH +*hv* → CH3O2 + OH + CO2	
PAN +*hv* → .6*CH3CO3 + .6*NO2 + .4*CH3O2 + .4*NO3 + .4*CO2	
MPAN +*hv* → MCO3 + NO2	
MACR +*hv* → .67*HO2 + .33*MCO3 + .67*CH2O + .67*CH3CO3 + .33*OH + .67*CO	
MVK +*hv* → .7*C3H6 + .7*CO + .3*CH3O2 + .3*CH3CO3	
C2H5OOH +*hv* → CH3CHO + HO2 + OH	
C3H7OOH +*hv* → .82*CH3COCH3 + OH + HO2	
ROOH +*hv* → CH3CO3 + CH2O + OH	
CH3COCH3 +*hv* → CH3CO3 + CH3O2	
CH3COCHO +*hv* → CH3CO3 + CO + HO2	
XOOH +*hv* → OH	
ONITR +*hv* → HO2 + CO + NO2 + CH2O	
ISOPOOH +*hv* → .402*MVK + .288*MACR + .69*CH2O + HO2	
HYAC +*hv* → CH3CO3 + HO2 + CH2O	
GLYALD +*hv* → 2*HO2 + CO + CH2O	
MEK +*hv* → CH3CO3 + C2H5O2	
BIGALD +*hv* → .45*CO + .13*GLYOXAL + .56*HO2 + .13*CH3CO3 + .18*CH3COCHO	
GLYOXAL +*hv* → 2*CO + 2*HO2	
ALKOOH +*hv* → .4*CH3CHO + .1*CH2O + .25*CH3COCH3 + .9*HO2 + .8*MEK + OH	
MEKOOH +*hv* → OH + CH3CO3 + CH3CHO	
TOLOOH +*hv* → OH + .45*GLYOXAL + .45*CH3COCHO + .9*BIGALD	
TERPOOH +*hv* → OH + .1*CH3COCH3 + HO2 + MVK + MACR	

Table 4. Continued.

Stratospheric only photolysis	Rate
CH4 +*hv* → H + CH3O2	
CH4 +*hv* → 1.44*H2 + .18*CH2O + .18*O + .66*OH + .44*CO2 + .38*CO + .05*H2O	
H2O +*hv* → OH + H	
H2O +*hv* → H2 + O1D	
H2O +*hv* → 2*H + O	
CL2 +*hv* → 2*CL	
OCLO +*hv* → O + CLO	
CL2O2 +*hv* → 2*CL	
HOCL +*hv* → OH + CL	
HCL +*hv* → H + CL	
CLONO2 +*hv* → CL + NO3	
CLONO2 +*hv* → CLO + NO2	
BRCL +*hv* → BR + CL	
BRO +*hv* → BR + O	
HOBR +*hv* → BR + OH	
BRONO2 +*hv* → BR + NO3	
BRONO2 +*hv* → BRO + NO2	
CH3CL +*hv* → CL + CH3O2	
CCL4 +*hv* → 4*CL	
CH3CCL3 +*hv* → 3*CL	
CFC11 +*hv* → 3*CL	
CFC12 +*hv* → 2*CL	
CFC113 +*hv* → 3*CL	
HCFC22 +*hv* → CL	
CH3BR +*hv* → BR + CH3O2	
CF3BR +*hv* → BR	
CF2CLBR +*hv* → BR + CL	
CO2 +*hv* → CO + O	
Odd-Oxygen Reactions	**Rate**
O + O2 + M → O3 + M	6E−34*(300/T)**2.4
O + O3 → 2*O2	8.00E−12*exp(−2060./T)
O + O + M → O2 + M	2.76E−34*exp(720./T)
O1D + N2 → O + N2	2.10E−11*exp(115./T)
O1D + O2 → O + O2	3.20E−11*exp(70./T)
O1D + H2O → 2*OH	2.20E−10
O1D + H2 → HO2 + OH	1.10E−10
O1D + N2O → N2 + O2	4.90E−11
O1D + N2O → 2*NO	6.70E−11
O1D + CH4 → CH3O2 + OH	1.13E−10
O1D + CH4 → CH2O + H + HO2	3.00E−11
O1D + CH4 → CH2O + H2	7.50E−12
O1D + HCN → OH	7.70E−11*exp(100./T)

Table 4. Continued.

Odd hydrogen reactions	Rate
H + O2 + M → HO2 + M	troe : ko = 4.40E−32*(300/T)**1.30 ki = 4.70E−11*(300/T)**0.20 f =0.60
H + O3 → OH + O2	1.40E−10*exp (−470./T)
H + HO2 → 2*OH	7.20E−11
H + HO2 → H2 + O2	6.90E−12
H + HO2 → H2O + O	1.60E−12
OH + O → H + O2	2.20E−11*exp(120./T)
OH + O3 → HO2 + O2	1.70E−12*exp(−940./T)
OH + HO2 → H2O + O2	4.80E−11*exp(250./T)
OH + OH → H2O + O	1.80E−12
OH + OH + M → H2O2 + M	troe : ko = 6.90E−31*(300/T)**1.00 ki = 2.60E−11 f =0.60
OH + H2 → H2O + H	2.80E−12*exp(−1800./T)
OH + H2O2 → H2O + HO2	1.80E−12
OH + HCN → HO2	troe : ko = 4.28E−33 ki = 9.30E−15*(300/T)**−4.42 f =0.80
OH + CH3CN → HO2	7.80E−13*exp(−1050./T)
HO2 + O → OH + O2	3.00E−11*exp(200./T)
HO2 + O3 → OH + 2*O2	1.00E−14*exp(−490./T)
HO2 + HO2 → H2O2 + O2	(2.3E−13*exp(600/T) + 1.7E−33 * [M] * exp(1000/T)) * (1 + 1.4E−21*[H2O]exp(2200/T))
H2O2 + O → OH + HO2	1.40E−12*exp(−2000./T)
Odd nitrogen reactions	**Rate**
N + O2 → NO + O	1.50E−11*exp(−3600./T)
N + NO → N2 + O	2.10E−11*exp(100./T)
N + NO2 → N2O + O	5.80E−12*exp(220./T)
NO + O + M → NO2 + M	troe : ko = 9.00E−32*(300/T)**1.50 ki = 3.00E−11 f =0.60
NO + HO2 → NO2 + OH	3.50E−12*exp(250./T)
NO + O3 → NO2 + O2	3.00E−12*exp(−1500./T)
NO2 + O → NO + O2	5.10E−12*exp(210./T)
NO2 + O + M → NO3 + M	troe : ko = 2.50E−31*(300/T)**1.80 ki = 2.20E−11*(300/T)**0.70 f =0.60
NO2 + O3 → NO3 + O2	1.20E−13*exp(−2450./T)
NO2 + NO3 + M → N2O5 + M	troe : ko = 2.00E−30*(300/T)**4.40 ki = 1.40E−12*(300/T)**0.70 f =0.60
N2O5 + M → NO2 + NO3 + M	k(NO2+NO3+M) * 3.333E26 * exp(10990/T)
NO2 + OH + M → HNO3 + M	troe : ko = 1.80E−30*(300/T)**3.00 ki = 2.80E−11 f =0.60
HNO3 + OH → NO3 + H2O	k0 + k3[M]/(1 + k3[M]/k2) k0 = 2.4E−14·exp(460/T) k2 = 2.7E−17·exp(2199/T) k3 = 6.5E−34·exp(1335/T)
NO3 + NO → 2*NO2	1.50E−11*exp(170./T)
NO3 + O → NO2 + O2	1.00E−11
NO3 + OH → HO2 + NO2	2.20E−11
NO3 + HO2 → OH + NO2 + O2	3.50E−12

Table 4. Continued.

NO2 + HO2 + *M* → HO2NO2 + M	troe : ko =2.00E−31*(300/T)**3.40 ki = 2.90E-12*(300/T)**1.10 *f* =0.60
HO2NO2 + OH → H2O + NO2 + O2	1.30E−12*exp(380./T)
HO2NO2 + M → HO2 + NO2 + M	k(NO2+HO2+M)·exp(−−10900/T)/2.1E−27
C-1 Degradation (Methane, CO, CH2O and derivatives)	**Rate**
CH4 + OH → CH3O2 + H2O	2.45E−12*exp(−1775./T)
CH3O2 + NO → CH2O + NO2 + HO2	2.80E−12*exp(300./T)
CH3O2 + HO2 → CH3OOH + O2	4.10E−13*exp(750./T)
CH3OOH + OH → CH3O2 + H2O	3.80E−12*exp(200./T)
CH2O + NO3 → CO + HO2 + HNO3	6.00E−13*exp(−2058./T)
CH2O + OH → CO + H2O + H	5.50E−12*exp(125./T)
CH2O + O → HO2 + OH + CO	3.40E−11*exp(−1600./T)
CO + OH + M → CO2 + HO2 + M	troe : ko = 5.90E−33*(300/T)**1.40 ki = 1.10E−12*(300/T)**−1.30 *f* = 0.60
CO + OH → CO2 + HO2	ki = 2.1E09 * (T/300)**6.1 ko = 1.5E−13 * (T/300)**0.6 rate = ko/(1+ko/(ki/M)) *0.6**(1/(1+log10(ko/(ki/M)**2)))
CH3O2 + CH3O2 → 2*CH2O + 2*HO2	5.00E−13*exp(−424./T)
CH3O2 + CH3O2 → CH2O + CH3OH	1.90E−14*exp(706./T)
CH3OH + OH → HO2 + CH2O	2.90E−12*exp(−345./T)
CH3OOH + OH → .7*CH3O2 + .3*OH + .3*CH2O + H2O	3.80E−12*exp(200./T)
HCOOH + OH → HO2 + CO2 + H2O	4.50E−13
CH2O + HO2 → HOCH2OO	9.70E−15*exp(625./T)
HOCH2OO → CH2O + HO2	2.40E+12*exp(−7000./T)
HOCH2OO + NO → HCOOH + NO2 + HO2	2.60E−12*exp(265./T)
HOCH2OO + HO2 → HCOOH	7.50E−13*exp(700./T)
C-2 Degradation	**Rate**
C2H2 + OH + M → .65*GLYOXAL + .65*OH + .35*HCOOH + .35*HO2 + .35*CO + M	troe : ko = 5.50E−30 ki = 8.30E−13*(300/T)**−2.00 *f* = 0.60
C2H6 + OH → C2H5O2 + H2O	8.70E−12*exp(−1070./T)
C2H4 + OH + M → .75*EO2 + .5*CH2O + .25*HO2 + M	troe : ko = 1.00E−28*(300/T)**0.80 ki = 8.80E−12 *f* = 0.60
C2H4 + O3 → CH2O + .12*HO2 + .5*CO + .12*OH + .5*HCOOH	1.20E−14*exp(−2630./T)
CH3COOH + OH → CH3O2 + CO2 + H2O	7.00E−13
C2H5O2 + NO → CH3CHO + HO2 + NO2	2.60E−12*exp(365./T)
C2H5O2 + HO2 → C2H5OOH + O2	7.50E−13*exp(700./T)
C2H5O2 + CH3O2 → .7*CH2O + .8*CH3CHO + HO2 + .3*CH3OH + .2*C2H5OH	2.00E−13
C2H5O2 + C2H5O2 → 1.6*CH3CHO + 1.2*HO2 + .4*C2H5OH	6.80E−14
C2H5OOH + OH → .5*C2H5O2 + .5*CH3CHO + .5*OH	3.80E−12*exp(200./T)
CH3CHO + OH → CH3CO3 + H2O	5.60E−12*exp(270./T)
CH3CHO + NO3 → CH3CO3 + HNO3	1.40E−12*exp(−1900./T)
CH3CO3 + NO → CH3O2 + CO2 + NO2	8.10E−12*exp(270./T)
CH3CO3 + NO2 + M → PAN + M	troe : ko = 8.50E−29*(300/T)**6.50 ki = 1.10E−11*(300/T) *f* = 0.60

Table 4. Continued.

CH3CO3 + HO2 → .75*CH3COOOH + .25*CH3COOH + .25*O3	4.30E−13*exp(1040./T)
CH3CO3 + CH3O2 → .9*CH3O2 + CH2O + .9*HO2 + .9*CO2 + .1*CH3COOH	2.00E−12*exp(500./T)
CH3CO3 + CH3CO3 → 2*CH3O2 + 2*CO2	2.50E−12*exp(500./T)
CH3COOOH + OH → .5*CH3CO3 + .5*CH2O + .5*CO2 + H2O	1.00E−12
EO2 + NO → EO + NO2	4.20E−12*exp(180./T)
EO + O2 → GLYALD + HO2	1.00E−14
EO → 2*CH2O + HO2	1.60E+11*exp(−4150./T)
GLYALD + OH → HO2 + .2*GLYOXAL + .8*CH2O + .8*CO2	1.00E−11
GLYOXAL + OH → HO2 + CO + CO2	1.10E−11
C2H5OH + OH → HO2 + CH3CHO	6.90E−12*exp(−230./T)
PAN + M → CH3CO3 + NO2 + M	k(CH3CO3+NO2+M) * 1.111E28 * exp(14000/T)
PAN + OH → CH2O + NO3	4.00E−14
C−3 Degradation	**Rate**
C3H6 + OH + M → PO2 + M	troe : ko = 8.00E−27*(300/T)**3.50 ki = 3.00E−11 $f = 0.50$
C3H6 + O3 → .54*CH2O + .19*HO2 + .33*OH + .08*CH4 + .56*CO + .5*CH3CHO + .31*CH3O2 + .25*CH3COOH	6.50E−15*exp(−1900./T)
C3H6 + NO3 → ONIT	4.60E−13*exp(−1156./T)
C3H7O2 + NO → .82*CH3COCH3 + NO2 + HO2 + .27*CH3CHO	4.20E−12*exp(180./T)
C3H7O2 + HO2 → C3H7OOH + O2	7.50E−13*exp(700./T)
C3H7O2 + CH3O2 → CH2O + HO2 + .82*CH3COCH3	3.75E−13*exp(−40./T)
C3H7OOH + OH → H2O + C3H7O2	3.80E−12*exp(200./T)
C3H8 + OH → C3H7O2 + H2O	1.00E−11*exp(−665./T)
PO2 + NO → CH3CHO + CH2O + HO2 + NO2	4.20E−12*exp(180./T)
PO2 + HO2 → POOH + O2	7.50E−13*exp(700./T)
POOH + OH → .5*PO2 + .5*OH + .5*HYAC + H2O	3.80E−12*exp(200./T)
CH3COCH3 + OH → RO2 + H2O	3.82E−11 * exp(2000/T) + 1.33E−13
RO2 + NO → CH3CO3 + CH2O + NO2	2.90E−12*exp(300./T)
RO2 + HO2 → ROOH + O2	8.60E−13*exp(700./T)
RO2 + CH3O2 → .3*CH3CO3 + .8*CH2O + .3*HO2 + .2*HYAC + .5*CH3COCHO + .5*CH3OH	7.10E−13*exp(500./T)
ROOH + OH → RO2 + H2O	3.80E−12*exp(200./T)
HYAC + OH → CH3COCHO + HO2	3.00E−12
CH3COCHO + OH → CH3CO3 + CO + H2O	8.40E−13*exp(830./T)
CH3COCHO + NO3 → HNO3 + CO + CH3CO3	1.40E−12*exp(−1860./T)
ONIT + OH → NO2 + CH3COCHO	6.80E−13
C−4 Degradation	**Rate**
BIGENE + OH → ENEO2	5.40E−11
ENEO2 + NO → CH3CHO + .5*CH2O + .5*CH3COCH3 + HO2 + NO2	4.20E−12*exp(180./T)
MVK + OH → MACRO2	4.13E−12*exp(452./T)
MVK + O3 → .8*CH2O + .95*CH3COCHO + .08*OH + .2*O3 + .06*HO2 + .05*CO + .04*CH3CHO	7.52E−16*exp(−1521./T)
MEK + OH → MEKO2	2.30E−12*exp(−170./T)
MEKO2 + NO → CH3CO3 + CH3CHO + NO2	4.20E−12*exp(180./T)
MEKO2 + HO2 → MEKOOH	7.50E−13*exp(700./T)
MEKOOH + OH → MEKO2	3.80E−12*exp(200./T)
MACR + OH → .5*MACRO2 + .5*H2O + .5*MCO3	1.86E−11*exp(175./T)

Table 4. Continued.

MACR + O3 → .8*CH3COCHO + .275*HO2 + .2*CO + .2*O3 + .7*CH2O + .215*OH	4.40E−15*exp(−2500./T)
MACRO2 + NO → NO2 + .47*HO2 + .25*CH2O + .53*GLYALD + .25*CH3COCHO + .53*CH3CO3 + .22*HYAC + .22*CO	2.70E−12*exp(360./T)
MACRO2 + NO → 0.8*ONITR	1.30E−13*exp(360./T)
MACRO2 + NO3 → NO2 + .47*HO2 + .25*CH2O + .25*CH3COCHO + .22*CO + .53*GLYALD + .22*HYAC + .53*CH3CO3	2.40E−12
MACRO2 + HO2 → MACROOH	8.00E−13*exp(700./T)
MACRO2 + CH3O2 → .73*HO2 + .88*CH2O + .11*CO + .24*CH3COCHO + .26*GLYALD + .26*CH3CO3 + .25*CH3OH + .23*HYAC	5.00E−13*exp(400./T)
MACRO2 + CH3CO3 → .25*CH3COCHO + CH3O2 + .22*CO + .47*HO2 + .53*GLYALD + .22*HYAC + .25*CH2O + .53*CH3CO3	1.40E−11
MACROOH + OH → .5*MCO3 + .2*MACRO2 + .1*OH + .2*HO2	2.30E−11*exp(200./T)
MCO3 + NO → NO2 + CH2O + CH3CO3	5.30E−12*exp(360./T)
MCO3 + NO3 → NO2 + CH2O + CH3CO3	5.00E−12
MCO3 + HO2 → .25*O3 + .25*CH3COOH + .75*CH3COOOH + .75*O2	4.30E−13*exp(1040./T)
MCO3 + CH3O2 → 2*CH2O + HO2 + CO2 + CH3CO3	2.00E−12*exp(500./T)
MCO3 + CH3CO3 → 2*CO2 + CH3O2 + CH2O + CH3CO3	4.60E−12*exp(530./T)
MCO3 + MCO3 → 2*CO2 + 2*CH2O + 2*CH3CO3	2.30E−12*exp(530./T)
MCO3 + NO2 + M → MPAN + M	1.1E−11 * 300/T/[M]
MPAN + M → MCO3 + NO2 + M	k(MCO3+NO2+M) * 1.111E28 * exp(14000/T)
MPAN + OH → .5*HYAC + .5*NO3 + .5*CH2O + .5*HO2	troe : ko = 8.00E−27*(300/T)**3.50 ki = 3.00E−11 $f = 0.50$

C−5 Degradation	Rate
ISOP + OH → ISOPO2	2.54E−11*exp(410./T)
ISOP + O3 → .4*MACR + .2*MVK + .07*C3H6 + .27*OH + .06*HO2 + .6*CH2O + .3*CO + .1*O3 + .2*MCO3 + .2*CH3COOH	1.05E−14*exp(−2000./T)
ISOP + NO3 → ISOPNO3	3.03E−12*exp(−446./T)
ISOPO2 + NO → .08*ONITR + .92*NO2 + HO2 + .51*CH2O + .23*MACR + .32*MVK + .37*HYDRALD	4.40E−12*exp(180./T)
ISOPO2 + NO3 → HO2 + NO2 + .6*CH2O + .25*MACR + .35*MVK + .4*HYDRALD	2.40E−12
ISOPO2 + HO2 → ISOPOOH	8.00E−13*exp(700./T)
ISOPOOH + OH → .8*XO2 + .2*ISOPO2	1.52E−11*exp(200./T)
ISOPO2 + CH3O2 → .25*CH3OH + HO2 + 1.2*CH2O + .19*MACR + .26*MVK + .3*HYDRALD	5.00E−13*exp(400./T)
ISOPO2 + CH3CO3 → CH3O2 + HO2 + .6*CH2O + .25*MACR + .35*MVK + .4*HYDRALD	1.40E−11
ISOPNO3 + NO → 1.206*NO2 + .794*HO2 + .072*CH2O + .167*MACR + .039*MVK + .794*ONITR	2.70E−12*exp(360./T)
ISOPNO3 + NO3 → 1.206*NO2 + .072*CH2O + .167*MACR + .039*MVK + .794*ONITR + .794*HO2	2.40E−12
ISOPNO3 + HO2 → XOOH + .206*NO2 + .794*HO2 + .008*CH2O + .167*MACR + .039*MVK + .794*ONITR	8.00E−13*exp(700./T)
BIGALK + OH → ALKO2	3.50E−12
ONITR + OH → HYDRALD + .4*NO2 + HO2	4.50E−11
ONITR + NO3 → HO2 + NO2 + HYDRALD	1.40E−12*exp(−1860./T)
HYDRALD + OH → XO2	1.86E−11*exp(175./T)
ALKO2 + NO → .4*CH3CHO + .1*CH2O + .25*CH3COCH3 + .9*HO2 + .8*MEK + .9*NO2 + .1*ONIT	4.20E−12*exp(180./T)
ALKO2 + HO2 → ALKOOH	7.50E−13*exp(700./T)

Table 4. Continued.

ALKOOH + OH → ALKO2	3.80E−12*exp(200./T)
XO2 + NO → NO2 + HO2 + .5*CO + .25*GLYOXAL + .25*HYAC + .25*CH3COCHO + .25*GLYALD	2.70E−12*exp(360./T)
XO2 + NO3 → NO2 + HO2 + 0.5*CO + .25*HYAC + 0.25*GLYOXAL + .25*CH3COCHO + .25*GLYALD	2.40E−12
XO2 + HO2 → XOOH	8.00E−13*exp(700./T)
XO2 + CH3O2 → .3*CH3OH + 0.8*HO2 + .7*CH2O + .2*CO + .1*HYAC + .1*GLYOXAL + .1*CH3COCHO + .1*GLYALD	5.00E−13*exp(400./T)
XO2 + CH3CO3 → 0.5*CO + CH3O2 + HO2 + CO2 + .25*GLYOXAL + .25*HYAC + .25*CH3COCHO + .25*GLYALD	1.30E−12*exp(640./T)
XOOH + OH → H2O + XO2	1.90E−12*exp(190./T)
XOOH + OH → H2O + OH	T**2 * 7.69E−17 * exp(253/T)
C-7 Degradation	**Rate**
TOLUENE + OH → .25*CRESOL + .25*HO2 + .7*TOLO2	1.70E−12*exp(352./T)
TOLO2 + NO → .45*GLYOXAL + .45*CH3COCHO + .9*BIGALD + .9*NO2 + .9*HO2	4.20E−12*exp(180./T)
TOLO2 + HO2 → TOLOOH	7.50E−13*exp(700./T)
TOLOOH + OH → TOLO2	3.80E−12*exp(200./T)
CRESOL + OH → XOH	3.00E−12
XOH + NO2 → .7*NO2 + .7*BIGALD + .7*HO2	1.00E−11
C-10 Degradation	**Rate**
C10H16 + OH → TERPO2	1.20E−11*exp(444./T)
C10H16 + O3 → .7*OH + MVK + MACR + HO2	1.00E−15*exp(−732./T)
C10H16 + NO3 → TERPO2 + NO2	1.20E−12*exp(490./T)
TERPO2 + NO → .1*CH3COCH3 + HO2 + MVK + MACR + NO2	4.20E−12*exp(180./T)
TERPO2 + HO2 → TERPOOH	7.50E−13*exp(700./T)
TERPOOH + OH → TERPO2	3.80E−12*exp(200./T)
Radon/Lead	**Rate**
Rn → Pb	2.10E−06
Aerosol precursors and aging	**Rate**
SO2+ OH → SO4	ko = 3.0E−31(300/T)3.3; ki = 1.E−12; $f = 0.6$
DMS + OH → SO2	9.60E−12*exp(−234./T)
DMS + OH → .5*SO2+ .5*HO2	1.7E−42 * exp(7810/T) * [M] * 0.21/ (1 + 5.5E−31 * exp(7460/T)* [M] * 0.21)
DMS + NO3 → SO2+ HNO3	1.90E−13*exp(520./T)
NH3 + OH → H2O	1.70E−12*exp(−710./T)
CB1 → CB2	7.10E−06
OC1 → OC2	7.10E−06

Table 4. Continued.

Heterogeneous reactions on tropospheric aerosols	Rate : γ = reaction probability
N2O5 → 2*HNO3	$\gamma = 0.1$ on OC, SO4, NH4NO3, SOA
NO3 → HNO3	$\gamma = 0.001$ on OC, SO4, NH4NO3, SOA
NO2 → 0.5*OH + 0.5*NO + 0.5*HNO3	$\gamma = 0.0001$ on OC, SO4, NH4NO3, SOA
HO2 → 0.5*H2O2	$\gamma = 0.2$ on OC, SO4, NH4NO3, SOA
O1D reactions with halogens	**Rate**
O1D + CFC11 → 3*CL	1.70E−10
O1D + CFC12 → 2*CL	1.20E−10
O1D + CFC113 → 3*CL	1.50E−10
O1D + HCFC22 → CL	7.20E−11
O1D + CCL4 → 4*CL	2.84E−10
O1D + CH3BR → BR	1.80E−10
O1D + CF2CLBR → BR	9.60E−11
O1D + CF3BR → BR	4.10E−11
Odd Chlorine Reactions	**Rate**
CL + O3 → CLO + O2	2.30E−11*exp(−200./T)
CL + H2 → HCL + H	3.05E−11*exp(−2270./T)
CL + H2O2 → HCL + HO2	1.10E−11*exp(−980./T)
CL + HO2 → HCL + O2	1.80E−11*exp(170./T)
CL + HO2 → OH + CLO	4.10E−11*exp(−450./T)
CL + CH2O → HCL + HO2 + CO	8.10E−11*exp(−30./T)
CL + CH4 → CH3O2 + HCL	7.30E−12*exp(−1280./T)
CLO + O → CL + O2	2.80E−11*exp(85./T)
CLO + OH → CL + HO2	7.40E−12*exp(270./T)
CLO + OH → HCL + O2	6.00E−13*exp(230./T)
CLO + HO2 → O2 + HOCL	2.70E−12*exp(220./T)
CLO + NO → NO2 + CL	6.40E−12*exp(290./T)
CLO + NO2 + M → CLONO2 + M	troe : ko = 1.80E−31*(300/T)**3.40 ki = 1.50E−11*(300/T)**1.90 $f = 0.60$
CLO + CLO → 2*CL + O2	3.00E−11*exp(−2450./T)
CLO + CLO → CL2 + O2	1.00E−12*exp(−1590./T)
CLO + CLO → CL + OCLO	3.50E−13*exp(−1370./T)
CLO + CLO + M → CL2O2 + M	troe : ko = 1.60E−32*(300/T)**4.50 ki = 2.00E−12*(300/T)**2.40 $f = 0.60$
CL2O2 + M → CLO + CLO + M	** User defined **
HCL + OH → H2O + CL	2.60E−12*exp(−350./T)
HCL + O → CL + OH	1.00E−11*exp(−3300./T)
HOCL + O → CLO + OH	1.70E−13
HOCL + CL → HCL + CLO	2.50E−12*exp(−130./T)
HOCL + OH → H2O + CLO	3.00E−12*exp(−500./T)
CLONO2 + O → CLO + NO3	2.90E−12*exp(−800./T)
CLONO2 + OH → HOCL + NO3	1.20E−12*exp(−330./T)
CLONO2 + CL → CL2 + NO3	6.50E−12*exp(135./T)

Table 4. Continued.

Odd Bromine Reactions	Rate
BR + O3 → BRO + O2	1.70E−11*exp(−800./T)
BR + HO2 → HBR + O2	4.80E−12*exp(−310./T)
BR + CH2O → HBR + HO2 + CO	1.70E−11*exp(−800./T)
BRO + O → BR + O2	1.90E−11*exp(230./T)
BRO + OH → BR + HO2	1.70E−11*exp(250./T)
BRO + HO2 → HOBR + O2	4.50E−12*exp(460./T)
BRO + NO → BR + NO2	8.80E−12*exp(260./T)
BRO + NO2 + M → BRONO2 + M	troe : ko = 5.20E−31*(300/T)**3.20 ki = 6.90E−12*(300/T)**2.90 f = 0.60
BRO + CLO → BR + OCLO	9.50E−13*exp(550./T)
BRO + CLO → BR + CL + O2	2.30E−12*exp(260./T)
BRO + CLO → BRCL + O2	4.10E−13*exp(290./T)
BRO + BRO → 2*BR + O2	1.50E−12*exp(230./T)
HBR + OH → BR + H2O	5.50E−12*exp(200./T)
HBR + O → BR + OH	5.80E−12*exp(−1500./T)
HOBR + O → BRO + OH	1.20E−10*exp(−430./T)
BRONO2 + O → BRO + NO3	1.90E−11*exp(215./T)
Organic Halogens Reactions with Cl, OH	**Rate**
CH3CL + CL → HO2 + CO + 2*HCL	2.17E−11*exp(−1130./T)
CH3CL + OH → CL + H2O + HO2	2.40E−12*exp(−1250./T)
CH3CCL3 + OH → H2O + 3*CL	1.64E−12*exp(−1520./T)
HCFC22 + OH → CL + H2O + CF2O	1.05E−12*exp(−1600./T)
CH3BR + OH → BR + H2O + HO2	2.35E−12*exp(−1300./T)
Sulfate aerosol reactions	**Comment**
N2O5 → 2*HNO3	$\gamma = 0.04$
CLONO2 → HOCL + HNO3	f (sulfuric acid wt%)
BRONO2 → HOBR + HNO3	f (T, P, HCl, H2O, r)
CLONO2 + HCL → CL2 + HNO3	f (T, P, H2O, r)
HOCL + HCL → CL2 + H2O	f (T, P, HCl, H2O, r)
HOBR + HCL → BRCL + H2O	f (T, P, HCl, HOBr,H2O, r)
Nitric acid di−hydrate reactions	**Comment**
N2O5 → 2*HNO3	$\gamma = 0.0004$
CLONO2 → HOCL + HNO3	$\gamma = 0.004$
CLONO2 + HCL → CL2 + HNO3	$\gamma = 0.2$
HOCL + HCL → CL2 + H2O	$\gamma = 0.1$
BRONO2 → HOBR + HNO3	$\gamma = 0.3$
Ice aerosol reactions	**Comment**
N2O5 → 2*HNO3	$\gamma = 0.02$
CLONO2 → HOCL + HNO3	$\gamma = 0.3$
BRONO2 → HOBR + HNO3	$\gamma = 0.3$
CLONO2 + HCL → CL2 + HNO3	$\gamma = 0.3$
HOCL + HCL → CL2 + H2O	$\gamma = 0.2$
HOBR + HCL → BRCL + H2O	$\gamma = 0.3$

Table 5. Bulk aerosol parameters used in calculation of surface area: number distribution mean radius (r_m), geometric standard deviation (σ_g) and density.

Aerosol	r_m (nm)	σ_g (μm)	ρ (g cm^{-3})
CB1, CB2	11.8	2.00	1.0
OC1, OC2	21.2	2.20	1.8
SO4	69.5	2.03	1.7
NH4NO3	69.5	2.03	1.7
SOA	21.2	2.20	1.8

While the lookup table provides explicit quantum yields and cross-sections for a large number of photolysis rate determinations, additional ones are available by scaling of any of the explicitly defined rates. This process is available in the definition of the chemical preprocessor input files (see Sect. 5 for a complete list of the photolysis rates available).

The impact of clouds on photolysis rates is parameterized following Madronich (1987). However, because we use a lookup table approach, the impact of aerosols (tropospheric or stratospheric) on photolysis rates cannot be represented.

4 Offline meteorology and transport

CAM-chem has the capability to perform simulations using specified dynamics, where offline meteorological fields are input into the model instead of calculated online. This procedure can allow for more precise comparisons between measurements of atmospheric composition and model output. To use input meteorological fields we follow the same procedure defined originally in the Model of Atmospheric Transport and Chemistry (MATCH) (Rasch et al., 1997) and subsequently applied in all versions of MOZART (E2010; Kinnison et al., 2007, Horowitz et al., 2003; Brasseur et al., 1998). In this procedure only the horizontal wind components, air temperature, surface temperature, surface pressure, sensible and latent heat flux and wind stress (see Table 2) are read from the input meteorological dataset; in all cases discussed here, the input datasets are available every 6 h. For timesteps between the reading times, all fields are linearly interpolated to avoid jumps. These fields are subsequently used to internally generate (using the existing CAM4 parameterizations) the variables necessary for (1) calculating subgrid scale transport including boundary layer transport and convective transport; (2) the variables necessary for specifying the hydrological cycle, including cloud and water vapor distributions and rainfall (see Rasch et al., 2007 for more details).

CAM4 (and therefore CAM-chem) uses a sub-stepping procedure to solve the advection equations for the mass flux, temperature and velocity fields over each timestep. Regardless of the configuration (online or specified dynamics), the meteorological fields are allowed to evolve over each substep. When using specified dynamics, we have found that this sub-stepping dampens some of the inconsistencies between the inserted and model-computed velocity and mass fields subsequently used for tracer transport. The mass flux (atmospheric mass and tracer mass) at each sub-step is accumulated to produce the net mass flux over the entire time step. This allows transport to be performed using a longer time step than the dynamics computations. A graphical explanation of the sub-stepping is given in Lauritzen et al. (2011).

In addition, an atmospheric mass fixer algorithm is necessary as the mass flux computed from the offline meteorological winds input into CAM4 will not in general produce a mass distribution consistent with the offline surface pressure field. If uncorrected this may lead to spurious changes in tracer mass, concentration or surface pressure (Rotman et al., 2004). The mass fixer algorithm ensures that the calculated surface pressure closely matches the surface pressure in the offline meteorological dataset (see discussion in Rotman et al., 2004). The mass fixer algorithm makes the appropriate adjustments to the horizontal mass fluxes to produce a resulting mass distribution consistent with the evolution of surface pressure in the input meteorological dataset. The procedure follows the algorithm given in Rotman et al. (2004): first it uses an efficient algorithm to find the correction to the vertically integrated mass flux, then the corrected mass flux is distributed in the vertical in proportion to the dependence of each model level on the surface pressure in a hybrid coordinate system. The edge pressures of the Lagrangian mass surfaces are consistently adjusted to allow for the vertical remapping of the transported fields to the fixed hybrid pressure coordinate system. Following the corrections in mass flux and the edge pressures the constituent tracers are transported by the large-scale wind fields.

Currently, we recommend using the NASA Goddard Global Modeling and Assimilation Office (GMAO) GEOS5 generated meteorology. The meteorological fields were generated using the operational forecast model and datasets (labeled below GEOS5) or under the Modern Era Retrospective-Analysis For Research And Applications (MERRA) setup (Rienecker et al., 2011). These differ in their assimilation methods and, to a lesser extent, assimilated datasets; see Rienecker et al. (2011) for more details. Using either of these meteorological datasets and the formulation of offline CAM-chem as described above, multi-year simulations (see Sect. 5 and Fig. 7) do not seem to require the use of limiters of stratosphere-troposphere exchange such as SYNOZ (McLinden et al., 2000). All GEOS5/MERRA meteorological datasets used in this study are made available at the standard CAM resolution of $1.9^\circ \times 2.5^\circ$ on the Earth System Grid (http://www.earthsystemgrid.org/home.htm). These files were generated from the original resolution ($1/2^\circ \times 2/3^\circ$) by using a conservative regridding procedure based on the same 1-D operators as used in the transport scheme of the finite-volume dynamical core used in

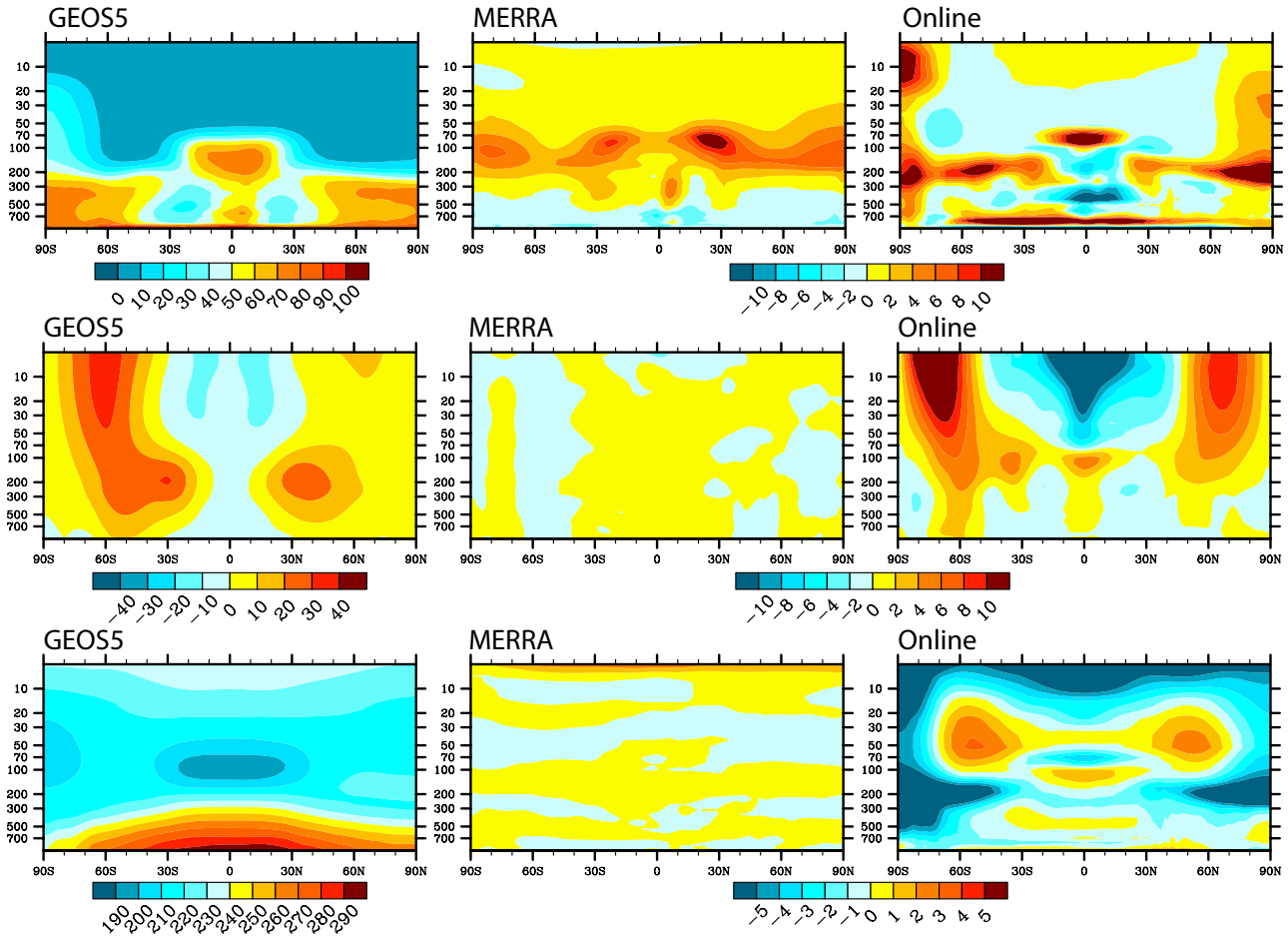

Fig. 4a. Annual (2006–2008) and zonal mean distribution of relative humidity (top, %), zonal wind (middle, m s^{-1}) and temperature (bottom, K) in GEOS5, MERRA and the online configurations (shown as absolute difference with respect to GEOS5, note different color scale).

GEOS5/MERRA and CAM (S.-J. Lin, personal communication, 2009). Note that because of a difference in the sign convention of the surface wind stress (TAUX and TAUY) between CESM and GEOS5/MERRA, these fields in the interpolated datasets have been reversed from the original files supplied by GMAO. In addition, it is important for users to recognize the importance of specifying the correct surface geopotential height (PHIS) to ensure consistency with the input dynamical fields, which is important to prevent unrealistic vertical mixing.

Over the range between the surface and 4 hPa, the number of vertical levels in the GEOS5/MERRA fields is 56, instead of 26 for the online dynamics (see Fig. 3). In particular, between 800 hPa and the surface, GEOS5/MERRA has 13 levels while the online version has 4. The choice of 26 levels is dictated by the use of CAM4 in climate simulations. No adjustment is made to the CAM4 physics parameterizations for this increase in the number of levels.

5 Chemical mechanisms

As mentioned in the Introduction, CAM-chem uses the same chemical preprocessor as MOZART-4. This preprocessor generates Fortran code specific to each chemical mechanism, allowing for an easy update and modification of existing chemical mechanisms. In particular, the generated code provides two chemical solvers, one explicit and one semi-implicit, which the user specifies based on the chemical lifetime of each species. Because the semi-implicit solver is quite efficient, it is recommended to preferentially use it unless the chemical species has a long lifetime everywhere.

We describe in this paper two chemical mechanisms, (1) extensive tropospheric chemistry, and (2) extensive tropospheric and stratospheric chemistry. All species and reactions are listed in Tables 3 and 4, respectively. In both mechanisms described in this paper, CAM-chem uses the bulk aerosol model discussed in Lamarque et al. (2005) and E2010. This model has a representation of aerosols based on the work by Tie et al. (2001, 2005), i.e., sulfate aerosol

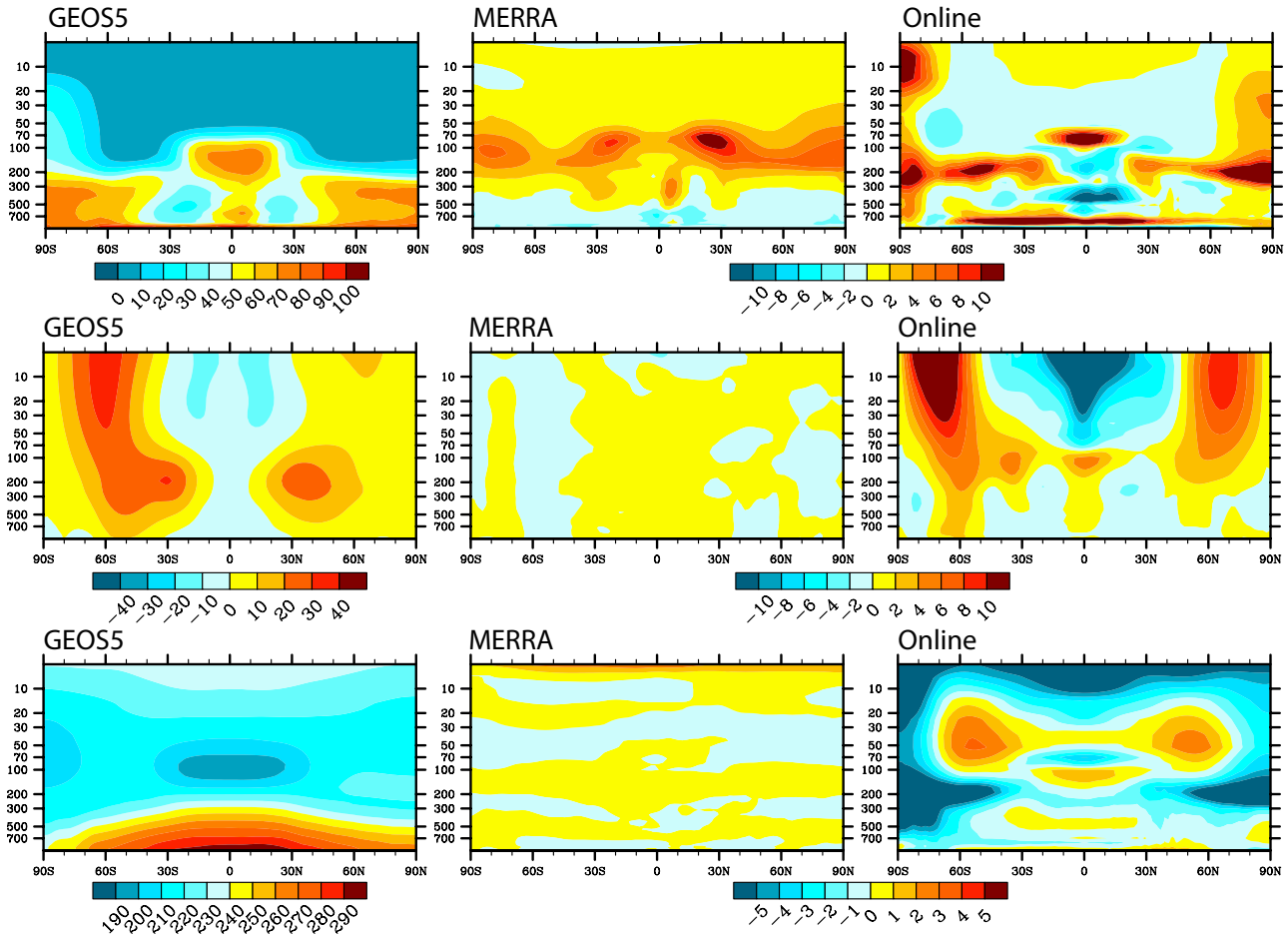

Fig. 4b. Annual (2006–2008) distribution of temperature at 700 hPa (top, K) and total precipitation (bottom, mm day^{-1}) in GEOS5, MERRA and the online configurations (shown as absolute difference with respect to GEOS5, note different color scale).

Table 6. Summary of simulations. All versions extend to ≈ 40 km.

Name	Dynamics	Period	Chemistry	Wet removal	Resolution	Levels
Online	online	1992–2010	stratosphere-troposphere	Neu and Prather	1.9° × 2.5°	26
GEOS5	GEOS5	2004–2010	troposphere	Horowitz	1.9° × 2.5°	56
MERRA	MERRA	1997–2010	troposphere	Horowitz	1.9° × 2.5°	56
MERRA Neu	MERRA	2006–2008	troposphere	Neu and Prather	1.9° × 2.5°	56

is formed by the oxidation of SO_2 in the gas phase (by reaction with the hydroxyl radical) and in the aqueous phase (by reaction with ozone and hydrogen peroxide). Furthermore, the model includes a representation of ammonium nitrate that is dependent on the amount of sulfate present in the air mass following the parameterization of gas/aerosol partitioning by Metzger et al. (2002). Because only the bulk mass is calculated, a lognormal distribution (Table 5, also see E2010) is assumed for all aerosols, with different mean radius and geometric standard deviation (Liao et al., 2003) for each aerosol type. The conversion of carbonaceous aerosols (organic and black) from hydrophobic to hydrophilic is assumed to occur within a fixed 1.6 days (Tie et al., 2005). Natural aerosols (desert dust and sea salt) are implemented following Mahowald et al. (2006a, b), and the sources of these aerosols are derived based on the model calculated wind speed and surface conditions. Size-dependent gravitational settling is included for dust and sea-salt. In addition, secondary-organic aerosols (SOA) are linked to the gas-phase chemistry through the oxidation of atmospheric non-methane hydrocarbons (NMHCs) as in Lack et al. (2004). Note that, because of the representation of SOA formation

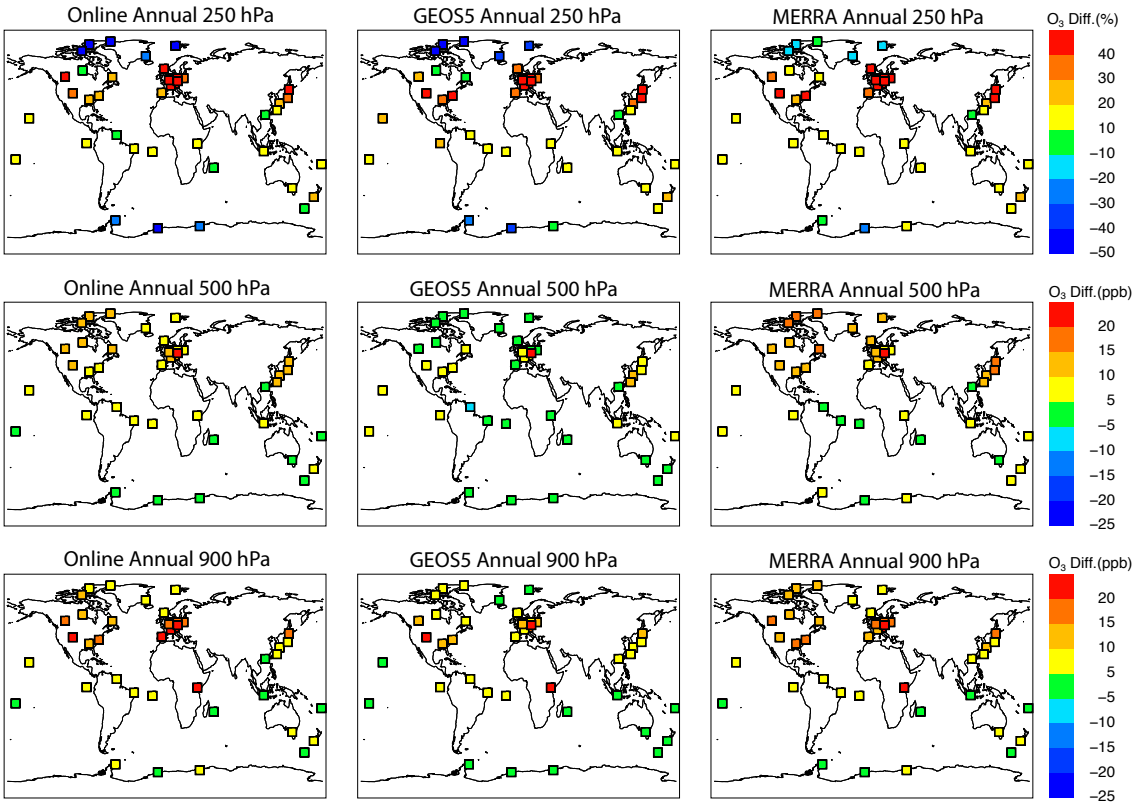

Fig. 5. Mean annual bias of modeled ozone against ozone sonde climatology (Tilmes et al., 2011) for 3 pressure levels; each square indicates the bias at the location of the ozone sonde. Averaging is done over the overlap period between the model simulations and the observations for each location.

through a 2-product method, there is no simple way to represent that in our chemical mechanism (and therefore Table 4); this calculation is therefore performed in a separate portion of the code, using information from the chemical mechanism (rate of VOC oxidation).

The extensive tropospheric chemistry scheme represents a minor update to the MOZART-4 mechanism, fully described in E2010. In particular, we have included chemical reactions for C_2H_2, HCOOH, HCN and CH_3CN and minor changes to the isoprene oxidation scheme, including an increase in the production of glyoxal. Reaction rates have been updated to JPL-2006 (Sander et al., 2006). This mechanism is mainly of relevance in the troposphere and is intended for simulations for which variability in the stratospheric composition is not crucial. Therefore, in this configuration, the stratospheric distributions of long-lived species (see discussion below) are specified from previously performed WACCM simulations (Garcia et al., 2007; see Sect. 6.3).

On the other hand, in the case where changes in stratospheric composition are important, for which the dynamics is calculated online, we have added a stratospheric portion to the tropospheric chemistry mechanism described above. This addition (of species and reactions, see Tables 3 and 4) is taken from the WACCM mechanism as this has been shown to perform very well in the recent CCMval-2 analysis (SPARC, 2010). The overall description of this chemistry is discussed in Kinnison et al. (2011).

6 Simulations setup, including emissions and other boundary conditions

All simulations discussed in this paper are performed at the horizontal resolution of 1.9° (latitude) and 2.5° (longitude). The number of vertical levels ranges from 26 levels (online dynamics) to 56 levels (GEOS5 and MERRA meteorology); in both cases, the model extends to approximately 4 hPa ($\approx$ 40 km). The computational cost of the various configurations scales (roughly) linearly with the number of tracers (103 for GEOS5/MERRA and 133 for online) and levels (56 for GEOS5/MERRA and 26 for online), leading to a cost for GEOS5/MERRA approximately 1.7 higher than the online configuration. The online simulation is performed using the Neu and Prather removal scheme, while the specified dynamics simulations are performed using the Horowitz wet removal scheme. Therefore, the label "MERRA" refers to the simulation with the Horowitz wet removal scheme; an

Table 7. Yearly emission totals (Tg(species) yr^{-1}).

Species	Sector	1997	1998	1999	2000	2001	2002	2002	2004	2005	2006	2007	2008	2009	2010
BIGALK	anthro	73.3	73.6	73.9	74.3	74.8	75.3	75.9	76.5	77.0	77.6	78.2	78.8	78.8	78.8
	bb	1.9	2.1	1.4	1.2	1.3	1.5	1.4	1.4	1.4	1.4	1.4	1.1	0.8	0.8
	total	75.2	75.7	75.3	75.5	76.0	76.8	77.3	77.9	78.5	79.0	79.6	79.9	79.5	79.6
BIGENE	anthro	7.1	7.1	7.1	7.2	7.3	7.4	7.5	7.5	7.6	7.7	7.7	7.8	7.8	7.8
	bb	2.3	2.3	1.2	0.9	1.0	1.4	1.3	1.4	1.4	1.4	1.4	0.9	2.0	2.1
	total	9.5	9.5	8.4	8.1	8.2	8.8	8.8	8.9	9.0	9.1	9.1	8.6	9.8	9.9
C10H16	biogenic	81.3	81.3	81.3	81.3	81.3	81.3	81.3	81.3	81.3	81.3	81.3	81.3	81.3	81.3
C2H2	anthro	3.4	3.4	3.4	3.4	3.4	3.4	3.4	3.4	3.4	3.4	3.4	3.4	3.4	3.4
	bb	0.3	0.3	0.2	0.2	0.2	0.2	0.2	0.2	0.3	0.2	0.2	0.2	0.7	0.7
	total	3.8	3.8	3.7	3.6	3.6	3.7	3.7	3.7	3.7	3.7	3.7	3.6	4.1	4.2
C2H4	anthro	6.7	6.7	6.7	6.7	6.8	7.0	7.1	7.2	7.2	7.3	7.4	7.5	7.5	7.5
	bb	8.8	8.4	5.6	4.6	5.1	5.8	5.4	6.0	6.1	5.8	6.0	4.3	3.0	3.1
	biogenic	5.0	5.0	5.0	5.0	5.0	5.0	5.0	5.0	5.0	5.0	5.0	5.0	5.0	5.0
	total	20.4	20.1	17.2	16.3	16.9	17.8	17.4	18.2	18.4	18.1	18.4	16.8	15.4	15.6
C2H5OH	anthro	5.4	5.4	5.4	5.4	5.4	5.4	5.4	5.4	5.4	5.4	5.4	5.4	5.4	5.4
	bb	0.6	0.6	0.4	0.4	0.4	0.5	0.4	0.5	0.5	0.4	0.5	0.4	0.0	0.0
	total	6.0	6.0	5.8	5.8	5.8	5.8	5.8	5.8	5.8	5.8	5.8	5.7	5.4	5.4
C2H6	anthro	7.5	7.5	7.5	7.5	7.6	7.6	7.7	7.7	7.8	7.8	7.9	7.9	7.9	7.9
	bb	4.9	4.5	2.8	2.3	2.5	3.0	2.7	3.2	3.2	3.1	3.1	2.1	1.7	1.9
	biogenic	1.0	1.0	1.0	1.0	1.0	1.0	1.0	1.0	1.0	1.0	1.0	1.0	1.0	1.0
	total	13.4	13.0	11.4	10.8	11.1	11.6	11.4	11.9	12.0	11.9	12.0	11.0	10.6	10.7
C3H6	anthro	2.8	2.8	2.8	2.8	2.8	2.9	2.9	2.9	3.0	3.0	3.0	3.1	3.1	3.1
	bb	2.6	2.8	1.8	1.5	1.6	1.9	1.9	1.9	1.9	1.8	1.9	1.4	1.6	1.8
	biogenic	1.0	1.0	1.0	1.0	1.0	1.0	1.0	1.0	1.0	1.0	1.0	1.0	1.0	1.0
	total	6.4	6.6	5.5	5.3	5.5	5.8	5.8	5.8	5.9	5.8	5.9	5.5	5.7	5.8
C3H8	anthro	7.9	8.0	8.0	8.0	8.1	8.2	8.2	8.3	8.3	8.4	8.5	8.5	8.5	8.5
	bb	0.8	0.9	0.6	0.5	0.5	0.6	0.6	0.6	0.6	0.6	0.6	0.5	0.4	0.4
	biogenic	2.0	2.0	2.0	2.0	2.0	2.0	2.0	2.0	2.0	2.0	2.0	2.0	2.0	2.0
	total	10.7	10.8	10.5	10.5	10.6	10.8	10.8	10.9	10.9	11.0	11.0	11.0	10.9	10.9
CB1	anthro	3.7	3.7	3.7	3.7	3.7	3.7	3.7	3.7	3.7	3.7	3.7	3.7	3.7	3.7
	bb	2.9	3.0	2.1	1.8	2.0	2.2	2.0	2.1	2.2	2.0	2.2	1.7	1.7	1.8
	total	6.6	6.7	5.8	5.5	5.7	5.9	5.8	5.9	5.9	5.8	5.9	5.4	5.4	5.5
CB2	anthro	0.9	0.9	0.9	0.9	0.9	0.9	0.9	0.9	0.9	0.9	0.9	0.9	0.9	0.9
	bb	0.7	0.8	0.5	0.5	0.5	0.5	0.5	0.5	0.5	0.5	0.5	0.4	0.4	0.4
	total	1.7	1.7	1.5	1.4	1.4	1.5	1.4	1.5	1.5	1.4	1.5	1.4	1.3	1.4
CH2O	anthro	0.9	0.9	0.9	1.0	1.0	1.0	1.0	1.0	1.0	1.1	1.1	1.1	1.1	1.1
	bb	4.2	4.9	2.7	2.2	2.3	3.1	3.1	2.8	2.8	2.9	2.8	2.1	4.4	4.7
	total	5.1	5.8	3.6	3.2	3.3	4.1	4.1	3.9	3.9	4.0	3.9	3.2	5.5	5.8
CH3CHO	anthro	2.1	2.1	2.1	2.1	2.2	2.2	2.2	2.2	2.2	2.2	2.2	2.2	2.2	2.2
	bb	7.6	8.2	5.5	4.8	5.1	5.8	5.6	5.6	5.7	5.4	5.7	4.5	4.6	4.7
	total	9.8	10.3	7.6	6.9	7.3	8.0	7.8	7.8	7.9	7.6	7.9	6.7	6.9	7.0
CH3CN	biofuel	0.7	0.7	0.7	0.7	0.7	0.7	0.7	0.7	0.7	0.7	0.7	0.7	0.7	0.7
	bb	1.6	1.7	1.1	1.0	1.1	1.2	1.2	1.2	1.2	1.1	1.2	0.9	1.1	1.2
	total	2.3	2.4	1.9	1.7	1.8	1.9	1.9	1.9	1.9	1.9	1.9	1.6	1.8	1.9
CH3COCH3	anthro	0.3	0.3	0.3	0.3	0.3	0.3	0.3	0.3	0.3	0.3	0.3	0.3	0.3	0.3
	bb	3.4	3.6	2.5	2.2	2.4	2.6	2.4	2.6	2.6	2.4	2.6	2.0	1.9	2.0
	biogenic	24.3	24.3	24.3	24.3	24.3	24.3	24.3	24.3	24.3	24.3	24.3	24.3	24.3	24.3
	total	28.1	28.2	27.1	26.8	27.0	27.3	27.1	27.2	27.3	27.1	27.3	26.7	26.6	26.7

Table 7. Continued.

species	sector	1997	1998	1999	2000	2001	2002	2002	2004	2005	2006	2007	2008	2009	2010
CH3COOH	anthro	6.6	6.6	6.6	6.6	6.6	6.6	6.6	6.6	6.6	6.6	6.6	6.6	6.6	6.6
	bb	3.1	2.7	1.8	1.5	1.5	2.0	1.9	2.0	2.2	2.1	2.1	1.6	8.1	8.5
	total	9.7	9.3	8.4	8.2	8.1	8.6	8.6	8.6	8.8	8.7	8.7	8.2	14.7	15.1
CH3OH	anthro	0.4	0.4	0.4	0.4	0.4	0.4	0.4	0.4	0.4	0.4	0.4	0.4	0.4	0.4
	bb	10.7	11.3	7.6	6.7	7.2	8.1	7.7	7.9	8.0	7.6	8.0	6.2	5.7	6.1
	biogenic	228.8	228.8	228.8	228.8	228.8	228.8	228.8	228.8	228.8	228.8	228.8	228.8	228.8	228.8
	total	239.9	240.5	236.8	235.8	236.4	237.3	236.9	237.1	237.2	236.8	237.2	235.4	234.9	235.3
CO	anthro	598.0	595.3	595.0	598.8	607.0	620.9	631.5	635.1	638.8	642.5	646.1	649.8	649.8	649.8
	bb	552.9	586.6	388.5	334.8	363.0	415.3	394.1	403.0	408.7	387.5	406.9	313.3	351.8	378.1
	biogenic	159.3	159.3	159.3	159.3	159.3	159.3	159.3	159.3	159.3	159.3	159.3	159.3	159.3	159.3
	ocean	19.8	19.8	19.8	19.8	19.8	19.8	19.8	19.8	19.8	19.8	19.8	19.8	19.8	19.8
	total	1330.1	1361.0	1162.6	1112.7	1149.1	1215.4	1204.8	1217.3	1226.7	1209.1	1232.2	1142.3	1180.8	1207.1
DMS	ocean	59.9	59.9	59.9	59.9	59.9	59.9	59.9	59.9	59.9	59.9	59.9	59.9	59.9	59.9
HCN	biofuel	1.0	1.0	1.0	1.0	1.0	1.0	1.0	1.0	1.0	1.0	1.0	1.0	1.0	1.0
	bb	2.2	2.4	1.6	1.4	1.5	1.7	1.6	1.6	1.7	1.6	1.6	1.3	1.3	1.4
	total	3.2	3.4	2.6	2.3	2.5	2.7	2.6	2.6	2.6	2.6	2.6	2.3	2.3	2.4
HCOOH	anthro	6.6	6.6	6.6	6.6	6.6	6.6	6.6	6.6	6.6	6.6	6.6	6.6	6.6	6.6
	bb	0.6	0.6	0.4	0.3	0.3	0.4	0.4	0.4	0.4	0.4	0.4	0.3	1.7	1.7
	total	7.2	7.2	7.0	6.9	6.9	7.0	7.0	7.0	7.1	7.0	7.0	7.0	8.3	8.3
MEK	anthro	1.2	1.2	1.2	1.3	1.3	1.3	1.3	1.3	1.3	1.4	1.4	1.4	1.4	1.4
	bb	7.4	7.9	5.2	4.5	4.9	5.6	5.3	5.4	5.5	5.2	5.5	4.2	4.7	5.0
	total	8.6	9.1	6.5	5.8	6.2	6.9	6.6	6.8	6.9	6.6	6.8	5.7	6.1	6.4
NH3	anthro	47.9	48.2	48.6	48.8	48.9	49.0	49.3	49.7	50.2	50.7	51.1	51.6	51.6	51.6
	bb	7.9	8.5	5.9	5.2	5.6	6.2	5.9	6.0	6.1	5.7	6.1	4.8	4.2	4.6
	ocean	8.1	8.1	8.1	8.1	8.1	8.1	8.1	8.1	8.1	8.1	8.1	8.1	8.1	8.1
	soil	2.4	2.4	2.4	2.4	2.4	2.4	2.4	2.4	2.4	2.4	2.4	2.4	2.4	2.4
	total	66.3	67.2	65.0	64.5	65.1	65.7	65.7	66.3	66.9	66.9	67.7	67.0	66.3	66.7
NO	anthro	59.3	59.7	60.3	60.9	61.6	62.9	63.9	64.4	64.9	65.4	65.9	66.5	66.5	66.5
	bb	14.0	16.0	11.4	10.4	11.1	12.0	11.6	11.3	11.5	10.7	11.5	9.7	5.5	5.9
	soil	17.1	17.1	17.1	17.1	17.1	17.1	17.1	17.1	17.1	17.1	17.1	17.1	17.1	17.1
	total	90.4	92.8	88.7	88.3	89.8	91.9	92.6	92.8	93.5	93.2	94.5	93.2	89.0	89.4
OC1	anthro	8.1	8.1	8.1	8.1	8.1	8.1	8.1	8.1	8.1	8.1	8.1	8.1	8.1	8.1
	bb	14.5	17.1	10.6	9.2	9.7	11.7	11.6	10.7	10.8	10.6	10.9	8.7	10.9	11.8
	total	22.5	25.1	18.6	17.3	17.8	19.8	19.7	18.8	18.8	18.6	18.9	16.8	19.0	19.8
OC2	anthro	8.1	8.1	8.1	8.1	8.1	8.1	8.1	8.1	8.1	8.1	8.1	8.1	8.1	8.1
	bb	14.5	17.1	10.6	9.2	9.7	11.7	11.6	10.7	10.8	10.6	10.9	8.7	10.9	11.8
	total	22.5	25.1	18.6	17.3	17.8	19.8	19.7	18.8	18.8	18.6	18.9	16.8	19.0	19.8
SO2	anthro	129.0	128.6	128.8	130.3	132.8	136.7	139.2	139.2	139.1	139.1	139.0	139.0	139.0	139.0
	bb	3.2	3.7	2.3	2.0	2.1	2.6	2.5	2.3	2.4	2.3	2.4	1.9	2.3	2.5
	volcano	9.5	9.5	9.5	9.5	9.5	9.5	9.5	9.5	9.5	9.5	9.5	9.5	9.5	9.5
	total	141.7	141.9	140.7	141.9	144.5	148.8	151.3	151.1	151.0	150.9	150.9	150.4	150.8	151.0
TOLUENE	anthro	28.7	28.8	29.0	29.2	29.5	30.0	30.4	30.8	31.2	31.6	32.0	32.4	32.4	32.4
	bb	3.8	4.5	2.8	2.5	2.6	3.1	3.1	2.9	2.9	2.8	2.9	2.3	11.8	12.6
	total	32.5	33.3	31.8	31.7	32.2	33.1	33.5	33.7	34.1	34.4	34.9	34.7	44.2	45.0

additional simulation (2006–2008) with MERRA but with the Neu and Prather wet removal scheme is labeled MERRA Neu. A summary is provided in Table 6. We focus on the period post-Pinatubo to limit the influence of the eruption on the chemical composition and meteorology. The starting dates for the offline simulations are dictated by the availability of the respective meteorological datasets.

6.1 Emissions

Available with the distribution of the CAM-chem are emissions for tropospheric chemistry that are an extension of the datasets discussed in E2010, covering 1992–2010. More specifically, for 1992–1996, which is prior to satellite-based fire inventories, monthly mean averages of the fire emissions for 1997–2008 from GFED2 (van der Werf et al., 2006 and updates) are used for each year. For 2009–2010, fire emissions are from FINN (Fire INventory from NCAR) (Wiedinmyer et al., 2010). As discussed in E2010, most of the anthropogenic emissions come from the POET (Precursors of Ozone and their Effects in the Troposphere) database for 2000 (Granier et al., 2005). The anthropogenic emissions (from fossil fuel and biofuel combustion) of black and organic carbon determined for 1996 are from Bond et al. (2004). For SO_2 and NH_3, anthropogenic emissions are from the EDGAR-FT2000 and EDGAR-2 databases, respec-

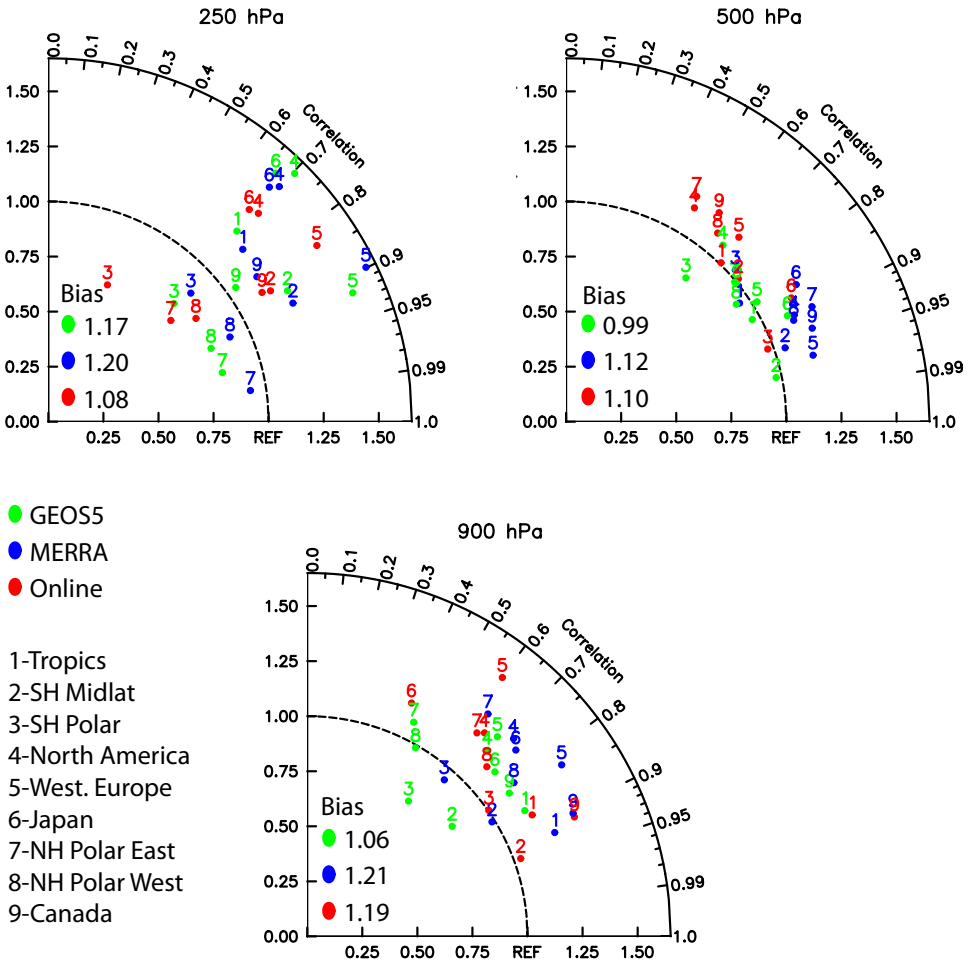

Fig. 6. Taylor diagram of modeled ozone against ozone sonde climatology (Tilmes et al., 2011) for 3 pressure levels; the radial distance indicates the normalized bias while the angle indicates the correlation of the average seasonal cycle. Averaging is done over the overlap period between the model simulations and the observations for each location.

tively (http://www.mnp.nl/edgar/). For Asia, these inventories have been replaced by the Regional Emission inventory for Asia (REAS) with the corresponding annual inventory for each year simulated (Ohara et al., 2007). Aircraft emissions have global annual totals of 0.63 Tg yr^{-1} (1.35 Tg N yr^{-1}) for NO, 1.70 Tg yr^{-1} for CO and 0.16 Tg yr^{-1} for SO_2. For the anthropogenic emissions, only Asian emissions (from REAS) are available each year, all other emissions are therefore repeated annually for each year of simulation. The DMS emissions are monthly means from the marine biogeochemistry model HAMOCC5, representative of the year 2000 (Kloster et al., 2006). SO_2 emissions from continuously outgassing volcanoes are from the GEIAv1 inventory (Andres and Kasgnoc, 1998). Totals for each year and emitted species are listed in Table 7. All emissions but volcanoes are released in the model bottom layer and implemented as a flux boundary condition for the vertical diffusion.

Note that while the emissions are provided at the model resolution, any emissions resolution can be used and the model automatically interpolates to the model resolution. At this point, this interpolation is a simple bilinear interpolation and therefore does not ensure exact conservation of emissions between resolutions. Errors are usually small and limited to areas of strong gradients.

6.2 Lower boundary conditions

For all long-lived species (see Table 3), the surface concentrations are specified using the historical reconstruction from Meinshausen et al. (2011). In addition, for CO_2 and CH_4, an observationally-based seasonal cycle and latitudinal gradient are imposed on the annual average values provided by Meinshausen et al. (2011). These values are used in the model by overwriting at each time step the corresponding model mixing ratio in the lowest model level with the time (and latitude, if applicable) interpolated specified mixing ratio.

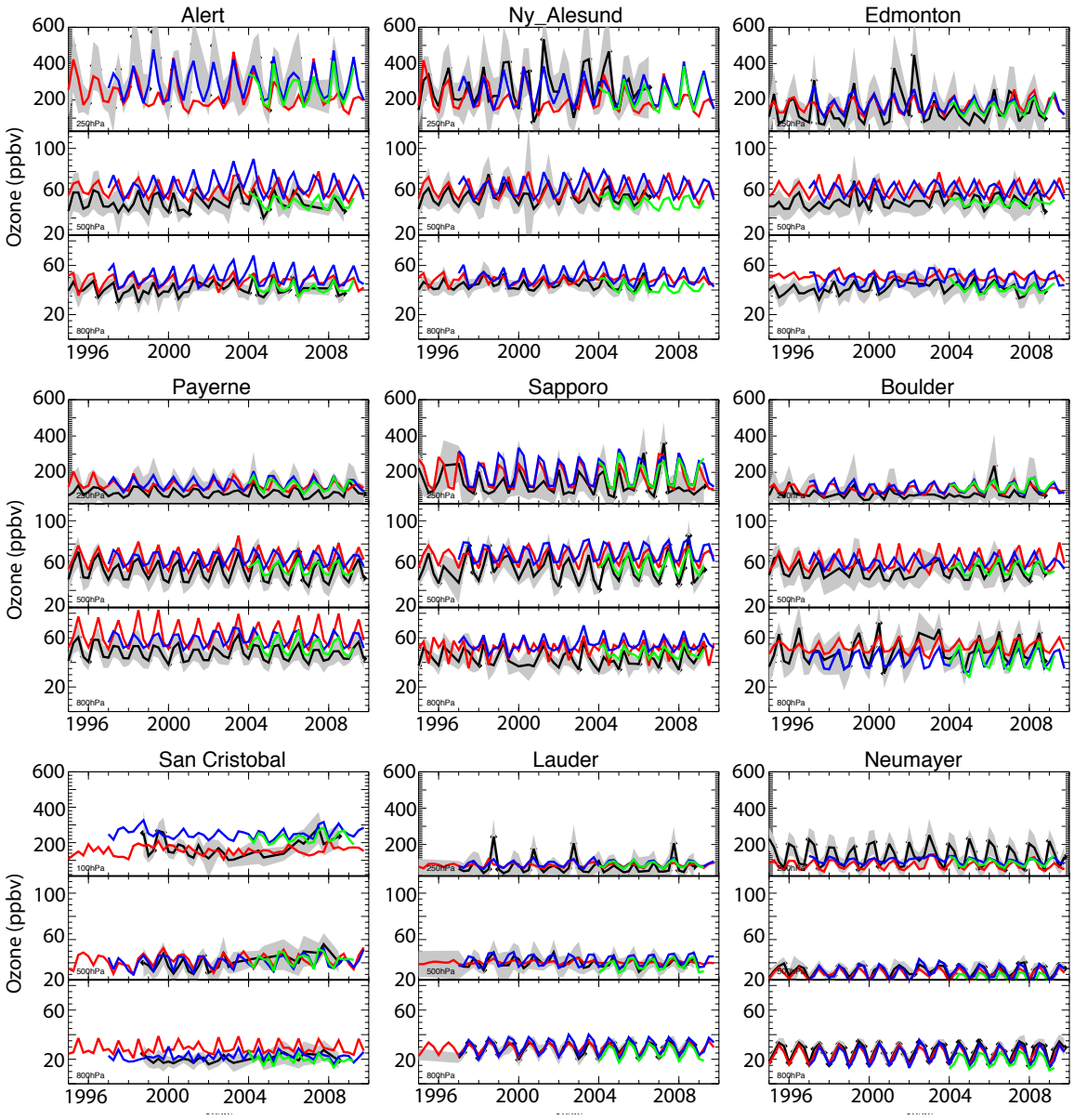

Fig. 7. Long-term change in median observed (grey shading indicates variability within the season) and simulated tropospheric ozone (top: 250 hPa, middle: 500 hPa and bottom: 800 hPa) for a variety of stations spanning the globe. Seasonal averages are shown. Black line is observations, red line is online, green line is GEOS5 and blue line is MERRA.

6.3 Specified stratospheric distributions

In the case where no stratospheric chemistry is explicitly represented in the model, it is necessary to ensure a proper distribution of some chemically-active stratospheric (namely O_3, NO, NO_2, HNO_3, CO, CH_4, N_2O, and N_2O_5) species, as is the case for MOZART-4. This monthly-mean climatological distribution is obtained from WACCM simulations covering 1950–2005 (Garcia et al., 2007). Because of the vast changes that occur over that time period, our data distribution provides files for three separate periods: 1950–1959, 1980–1989 and 1996–2005. This ensures that users can perform simulations with a stratospheric climatology representative of the pre-CFC era, as well as during the high CFC and post-Pinatubo era. Note that additional datasets can easily be constructed if necessary.

While transport and chemistry are applied to all species in the stratosphere, the concentration of the species listed above are explicitly overwritten from the model top to 50 hPa. Between that level and two model levels above the tropopause (computed from the temperature profile), a 10-day relaxation is applied to force the model concentrations towards the observations.

Table 8. Bias (ppb) and correlation coefficient (r) of ozone timelines between ozone sonde observations and model results for a matching time period.

Sites	Configuration	800 hPa	500 hPa	250 hPa
Alert	online	9.25/0.74	11.06/0.57	−60.25/0.45
	MERRA	11.62/0.88	14.43/0.69	12.24/0.76
	GEOS5	1.03/0.72	4.11/0.68	−28.18/0.84
NyAlesund	online	4.83/0.45	5.42/0.75	−68.21/0.54
	MERRA	5.99/0.77	8.98/0.49	3.16/0.69
	GEOS5	−0.40/0.78	−1.31/0.77	−19.12/0.48
Edmonton	online	10.77/0.36	11.24/0.65	46.60/0.68
	MERRA	10.81/0.68	10.17/0.50	57.91/0.76
	GEOS5	−0.64/0.86	−1.78/0.83	22.52/0.70
Payerne	online	13.73/0.76	7.63/0.87	38.70/0.44
	MERRA	9.67/0.86	11.86/0.73	46.08/0.65
	GEOS5	2.30/0.92	2.80/0.92	41.84/0.73
Sapporo	online	11.04/0.25	13.97/0.79	73.98/0.73
	MERRA	12.25/0.64	17.88/0.77	127.97/0.75
	GEOS5	4.91/0.72	2.53/0.90	117.67/0.63
Boulder	online	4.07/0.78	6.72/0.71	22.98/0.45
	MERRA	−2.46/0.82	7.86/0.67	21.68/0.55
	GEOS5	−2.83/0.86	3.95/0.85	31.10/0.64
Sancristobal	online	8.59/0.04	4.40/0.69	5.33/0.63
	MERRA	3.30/0.12	4.53/0.75	13.00/0.74
	GEOS5	−3.37/0.08	−0.56/0.67	10.86/0.74
Lauder	online	−0.68/0.91	1.65/0.68	22.95/0.41
	MERRA	0.86/0.92	5.44/0.60	26.25/0.63
	GEOS5	−3.18/0.92	2.19/0.78	30.35/0.66
Neumayer	online	−1.48/0.95	−3.14/0.85	−53.98/0.70
	MERRA	−3.35/0.91	−1.59/0.88	−19.76/0.81
	GEOS5	−11.68/0.87	−8.15/0.87	−44.51/0.89

7 Comparison with observations

The purpose of this section is to document the model chemistry performance against observations for the model setups described in Sect. 6 (see Table 6 for a summary). Model performance in simulating climate and meteorological features can be found in Lamarque et al. (2008), Lamarque and Solomon (2010) and in Neale et al. (2011). Here, we contrast the fields generated by CAM4 in the simulations listed in Table 6.

The zonal mean distribution (Fig. 4a) of relative humidity is very similar between GEOS5 (considered here as the reference since it is the operational forecast product and assimilates the most observations) and MERRA, except in the Northern Hemisphere polar stratosphere and in the lower troposphere, where MERRA is slightly drier than GEOS5 (not shown). On the other hand, it is clear that the online distribution is wetter in the tropical lower troposphere, and drier in the tropical upper troposphere.

The zonal mean wind is essentially the same in the GEOS5 and MERRA simulations, but the online polar jets are stronger in both hemispheres, leading to a more isolated polar stratosphere. Other features, such as the position and strength of the mid-latitude jet, are very similar between the simulations.

In terms of temperature, the online configuration is characterized by a slightly higher-altitude tropical minimum, as well as a colder Southern Hemisphere polar stratosphere, related to the stronger jet. We also find that the online simulation tends to be colder in the Northern polar lower stratosphere. The online produces a shift of the tropical tropopause, with a warming in the upper-troposphere and cooling in the lower stratosphere, similar to the findings of Collins et al. (2011) when using interactive ozone. In the lower troposphere (700 hPa, Fig. 4b), there is no clear indication of a bias, except for slightly warmer land areas of the Northern Hemisphere (1–2 K, not shown) in online compared to GEOS5/MERRA.

Many of the precipitation patterns are similar between the configurations (Fig. 4b), but the difference with respect to GEOS5 indicates that MERRA has slightly different tropical structure (stronger precipitation) while the online configuration has an overall stronger precipitation in both the tropical and midlatitude ocean regions. Land masses tend to be drier in the online version, except for Central Africa, China and the Himalayas.

The chemical composition evaluation below makes use of a variety of measurements: surface, airborne and satellite. In the case of the online stratosphere-troposphere version, the comparison will include evaluation of modeled total ozone column. It is important to note that, because the online model is only driven by the observed sea-surface temperatures, there is no expectation that a single-year in the model simulation will be directly comparable with observations; instead, the most meaningful comparison is at the climatological level.

7.1 Comparison with ozone: sondes and surface

Due to its central role in tropospheric chemistry and the availability of numerous ozone sonde measurements dating several decades (Logan, 1994), we focus our first evaluation on tropospheric ozone using ozone sonde measurements, both at specific locations and averaged over representative regions (supplement Fig. S1; Tilmes et al., 2011). For a variety of sites spanning the whole globe (especially in the meridional direction), the data coverage allows the comparison of profiles (Fig. S2), seasonal cycles (Fig. S3) and long-term changes (Fig. 7).

In order to provide a more concise description of the model performance under various configurations, we first display the annual bias at specific pressure levels (250 hPa, 500 hPa and 900 hPa) to span the troposphere and lower stratosphere (Fig. 5). In particular, at high latitudes, the 250 hPa surface will be located in the stratosphere during a fraction of the year.

We find that the model tends to underestimate the ozone concentration at 250 hPa in the high latitudes. On the other hand, most of the mid-latitude sites indicate a positive bias. This is an indication that the model seems to provide a position of the chemical tropopause that is lower than observed, i.e., an overestimate of the ozone mixing ratio in the lower stratosphere (i.e., 200–300 hPa, see Fig. 5). This is confirmed by the Taylor diagrams (generated using regional averages of ozone sondes and equivalent model results from monthly output), which indicate that all versions are quite similar at 250 hPa (Fig. 6). In particular, the seasonal cycle (quantified by the correlation coefficient, computed using monthly-averaged data and model output) ranges between 0.7 and 0.9, indicating a reasonable representation of ozone variations at 250 hPa.

At 500 hPa, GEOS5 is clearly providing the best performance, with many stations with a bias smaller in absolute value than 5 ppbv. It is interesting to note that MERRA behaves quite differently than GEOS5. This is most likely due to differences in the assimilation method and datasets used. In particular, as discussed below, the MERRA meteorology leads to a much stronger stratosphere-troposphere flux of ozone, likely leading to the 500 hPa biases. In terms of bias, the online simulation performs better than MERRA, especially in the Southern Hemisphere. However, the correlation is much worse (0.5–0.6) for many of the Northern Hemisphere stations. The seasonal cycle in both MERRA and GEOS5 seems equally good.

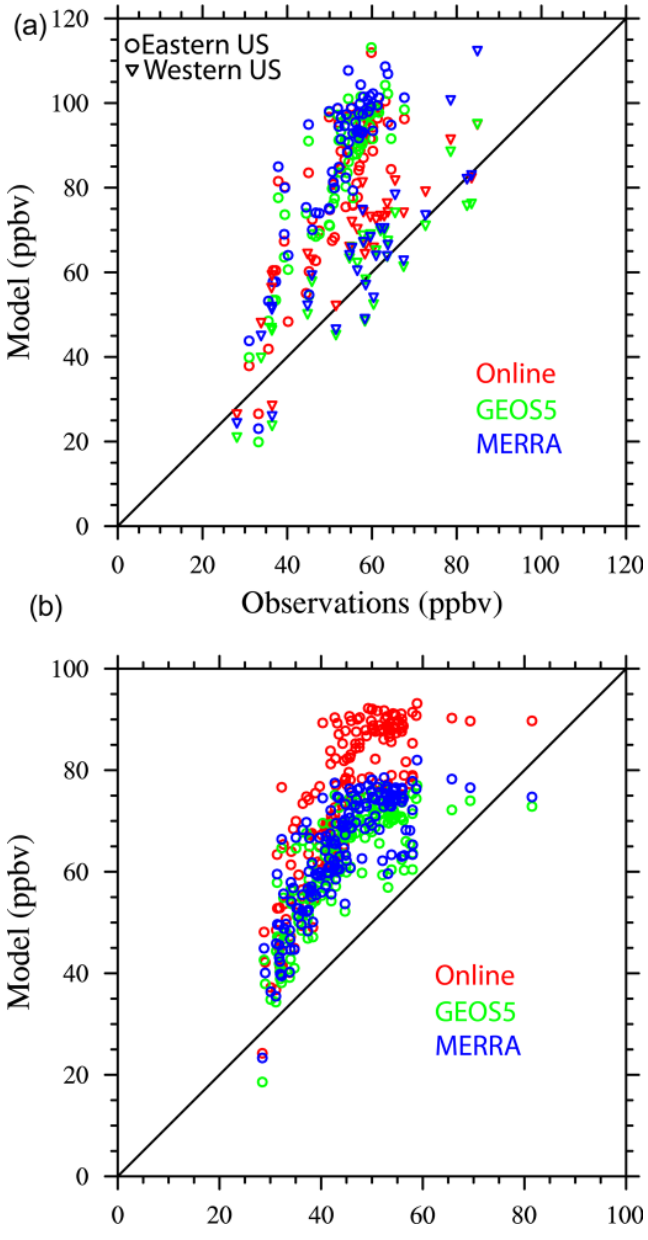

Fig. 8. **(a)** Comparison of surface ozone summertime 8-h maximum for CASTNET sites over the United States. **(b)** Same as **(a)** but for the European EMEP sites.

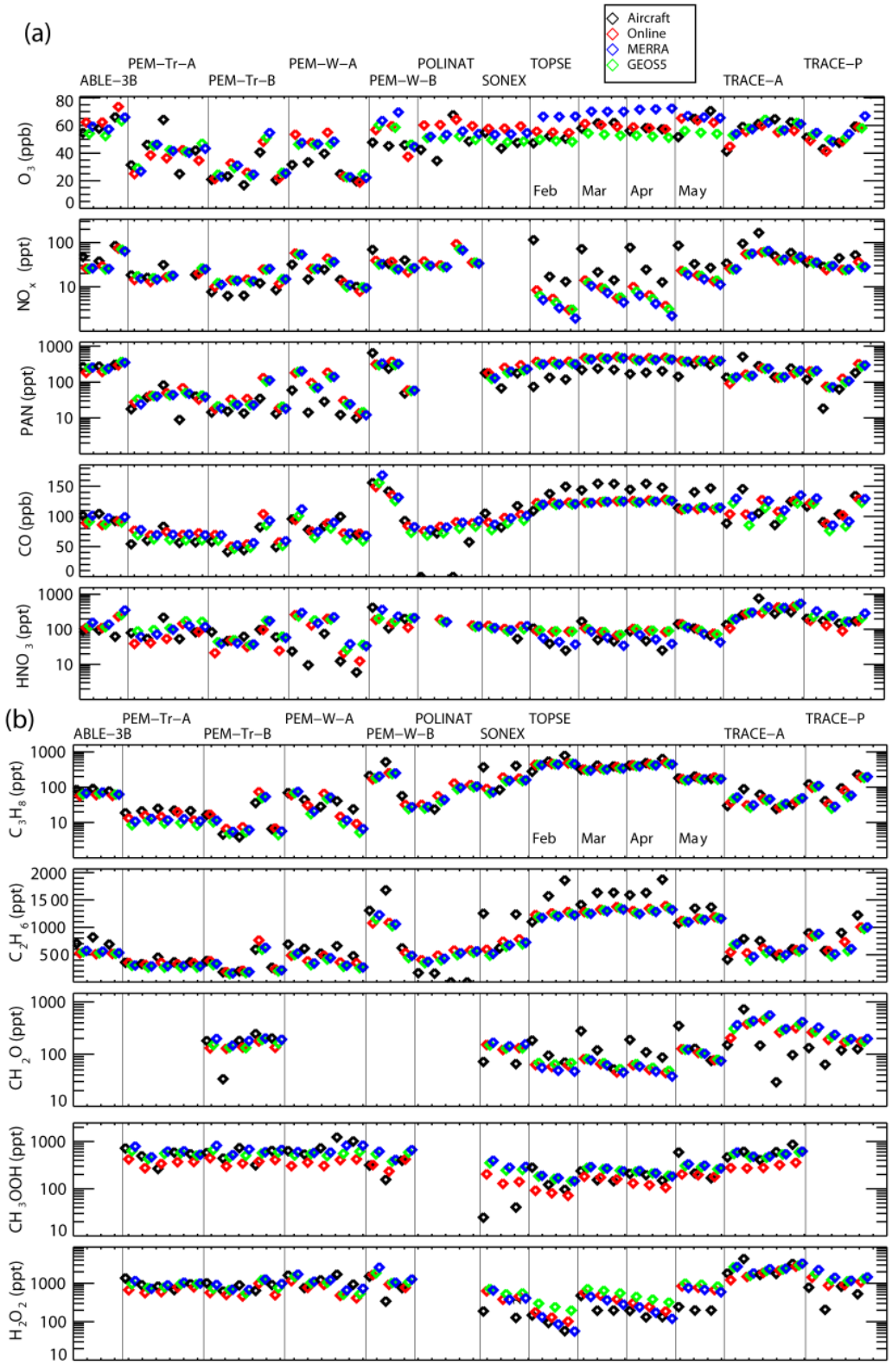

Fig. 9. **(a)** Comparison of regional aircraft profiles (from Emmons et al., 2000) averaged over 2–6 km to the online, GEOS5 and MERRA model simulations. Each symbol represents an aircraft campaign region in the climatology. **(b)** Same as **(a)** but for additional species.

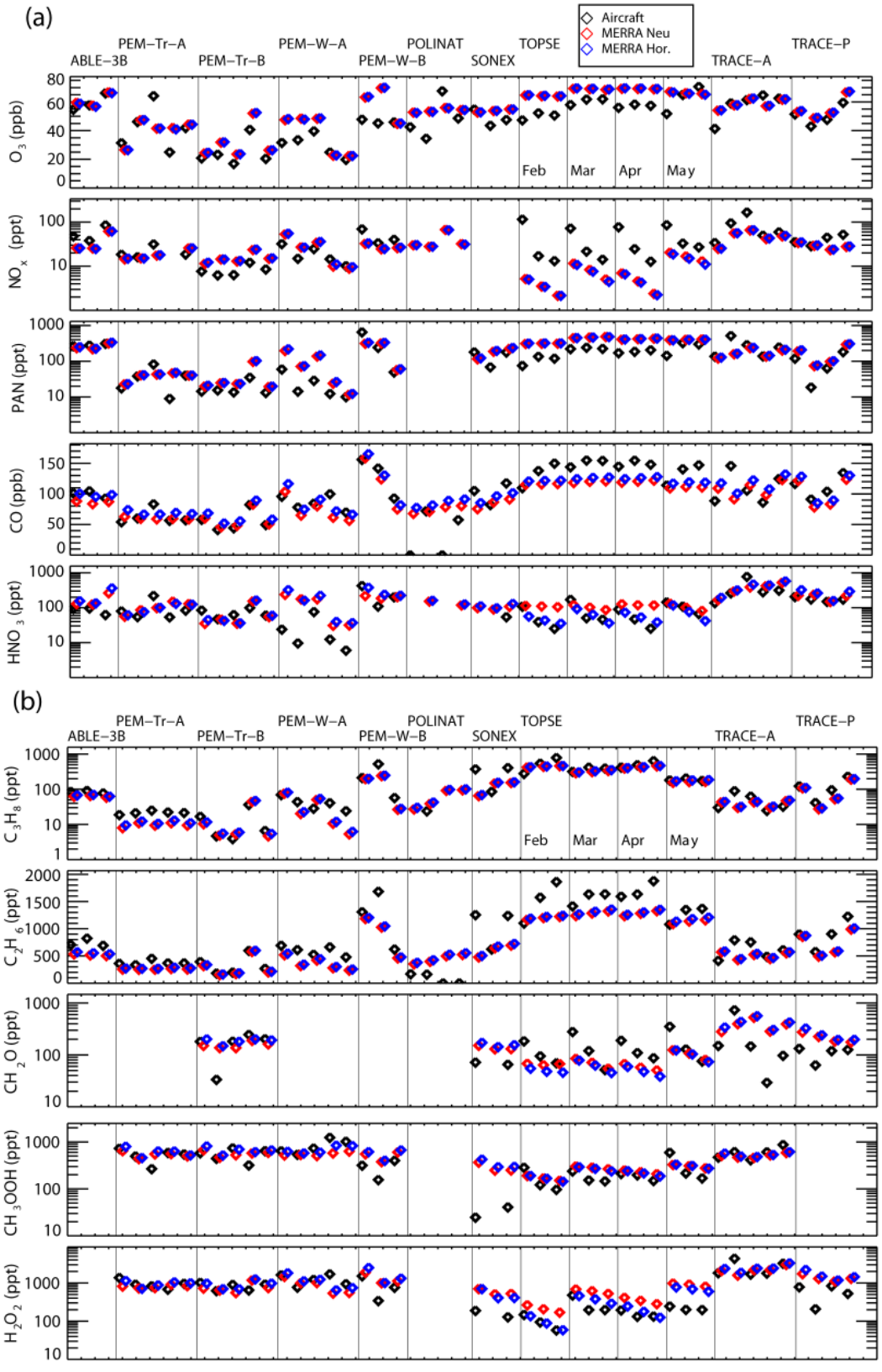

Fig. 10. **(a)** As Fig. 9a, except comparing the Horowitz and Neu and Prather washout schemes. **(b)** Same as **(a)** but for additional species.

Table 9. Tropospheric (ozone ≤ 100 ppb) ozone budget, methane lifetime, isoprene and lightning emissions averaged for 2006–2008.

Name Units	Burden Tg	Production Tg yr^{-1}	Loss Tg yr^{-1}	Net Chem. Tg yr^{-1}	Deposition Tg yr^{-1}	STE Tg yr^{-1}	Lifetime days	CH_4 lifetime years	Isoprene Tg yr^{-1}	Lightning TgN yr^{-1}
GEOS5	328	4897	4604	293	705	411	26.0	8.7	540	3.6
MERRA Neu	345	4778	4682	96	770	674	26.9	8.7	540	4.4
MERRA	346	4868	4760	108	781	673	26.5	9.1	540	4.4
Online	349	5014	4657	357	773	416	27.4	9.8	602	4.3

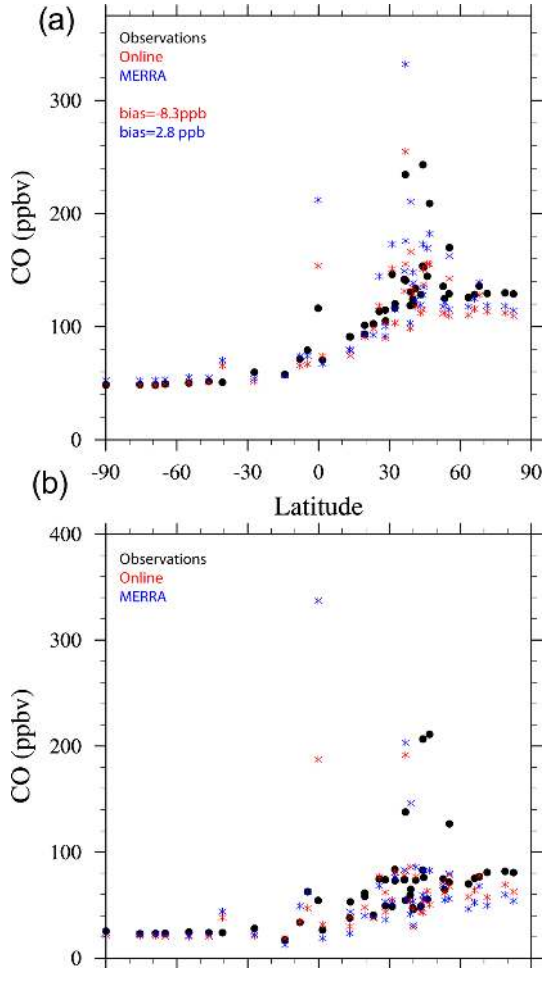

Fig. 11. **(a)** Comparison of the annual mean surface mixing ratio of CO to NOAA/GMD observations. **(b)** Comparison of the mean annual cycle (maximum minus minimum) of surface CO mixing ratio.

In the lower troposphere (900 hPa) the various configurations tend to exhibit similar regional annual biases, especially in the Northern Hemisphere. Correlation of the annual cycle is, for most regions, in the range 0.6–0.9, with some clear misrepresentations, especially the MERRA simulation over North America. Surface ozone is discussed below.

The analysis of long-term changes (Fig. 7) indicates that observed meteorology is important in representing interannual variability, especially in the upper troposphere, as the correlation for GEOS5/MERRA tends to be higher than in the online configuration (Table 8; stations were selected for the availability of fairly continuous long-term records). Nevertheless, from Table 8, the bias at 250 hPa seems to be better captured by the online simulation for the analysis stations equatorward of 40°, possibly related to consistently representing transport and chemistry. Overall, Table 8 confirms the previous analysis that, in the free troposphere (500 hPa), GEOS5 provides the best representation of ozone. That configuration also tends to provide a better simulation at 800 hPa, with a lower mean bias and usually high (>0.7) correlation coefficient. The seasonal cycle at the tropical station San Cristobal (Galapagos) is clearly misrepresented at that altitude in all configurations.

The annual budget for tropospheric ozone is summarized in Table 9; note that these are averaged numbers, with an interannual variability on the order of 10 %. We find that the online and offline versions have similar tropospheric (defined here as the region of the atmosphere where the ozone mixing ratio is lower than 100 ppbv) burdens and depositions, but with an overall smaller net chemical ozone production in the case of the offline meteorology. The corollary to this comparison is that the diagnosed stratosphere-troposphere flux of ozone (computed as the difference between the deposition and net chemical production) ranges from 410–420 Tg yr^{-1} (online and GEOS5) to 675 Tg yr^{-1} (MERRA), within the range of published model-derived estimates (e.g., 515–550 Tg yr^{-1}, Hsu et al., 2005; 556 ± 154 Tg yr^{-1}, Stevenson et al., 2005). In the case of the online simulation, this leads to an ozone lifetime of ≈ 27 days, in very good agreement with Stevenson et al. (2005).

To discuss surface ozone, we present in Fig. 8a and b the comparison of summertime (June–August) daily 8-h maximum (usually afternoon) for the United States (from the CASTNET network) and Europe (from the EMEP network). Because of the very different chemical regimes between Western and Eastern United States, we have separated the stations using longitude 100° W as the line of demarcation. We find that all model configurations tend to reproduce the Western sites quite well, with a propensity for the online

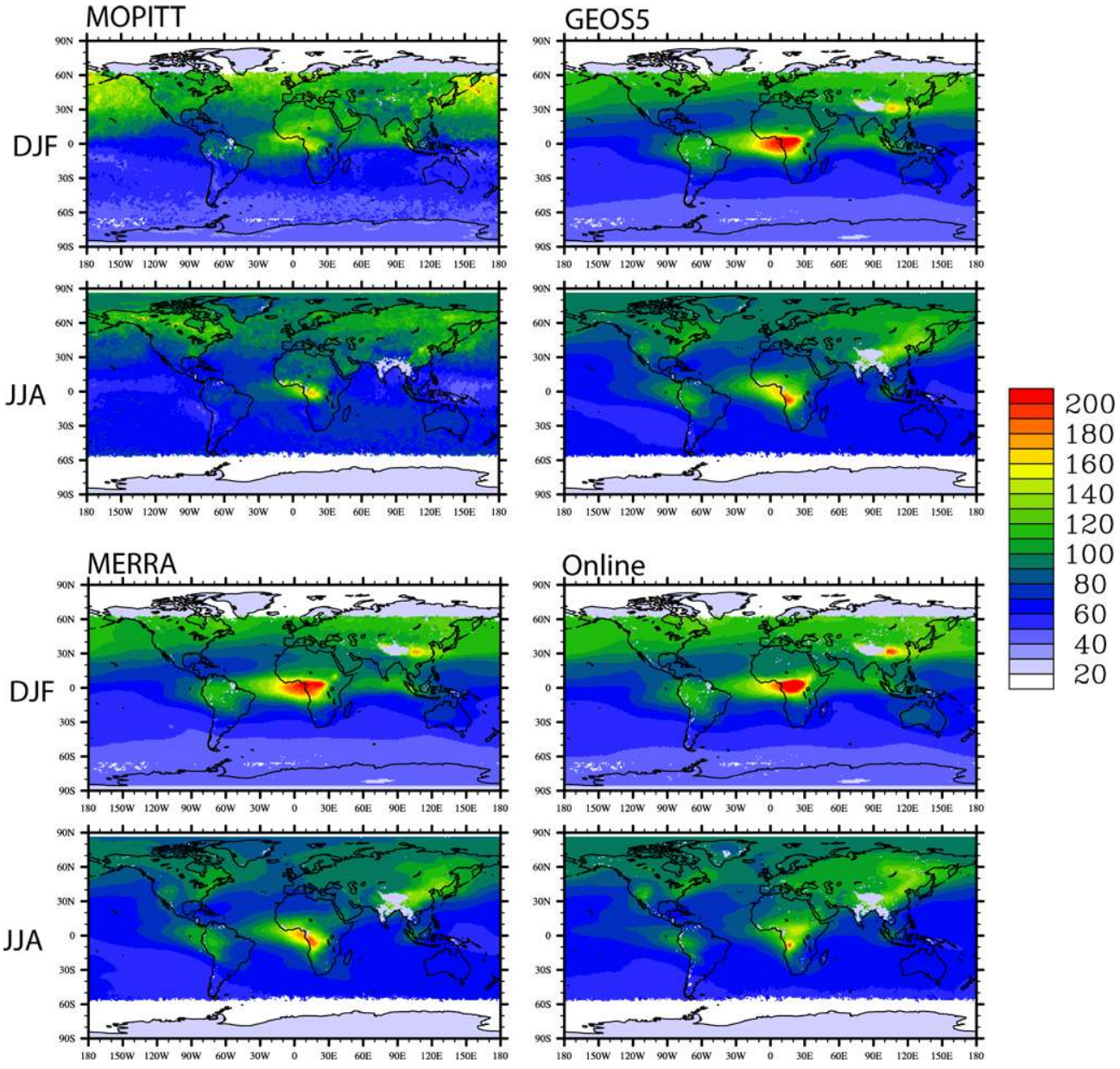

Fig. 12. Comparison of MOPITT (2004–2009) climatology of day-time CO (ppbv) retrievals at 500 hPa with model results (convolved with a priori and averaging kernels) for winter (DJF) and summer (JJA). Model results are averaged over the same period.

Table 10. CO evaluation against NOAA/GMD stations.

	Annual mean bias (ppb)	Annual mean rmsd (ppb)	Annual mean correl.	Seasonal cycle bias (ppb)	Seasonal cycle rmsd (ppb)	Seasonal cycle correl.
MERRA	2.8	28	0.99	−3.8	53	0.47
Online	−8.3	22	0.80	−8.5	40	0.37

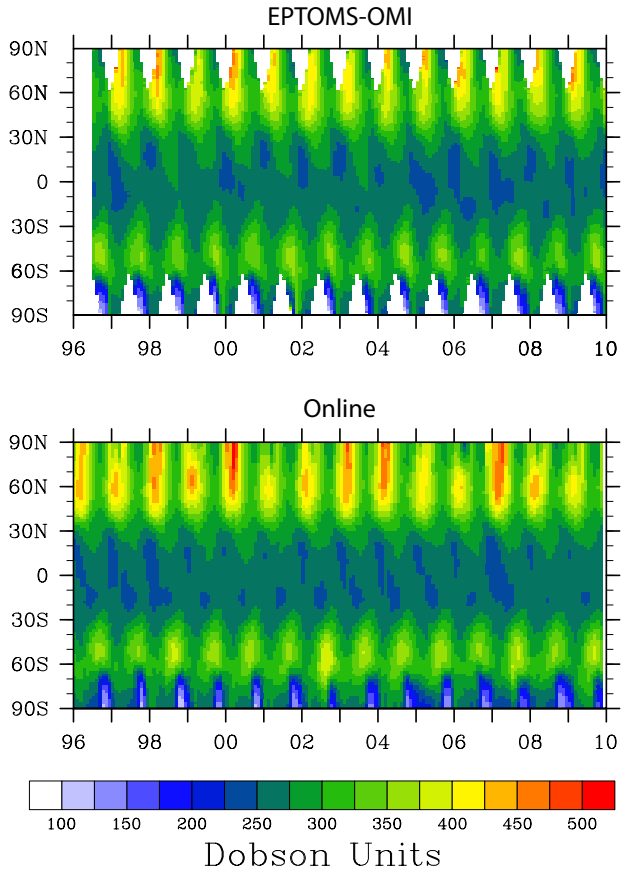

Fig. 13. Time evolution of zonally and monthly-averaged total ozone column (in Dobson Units) from satellite measurements (EP-TOMS and OMI, top) and online simulation (bottom).

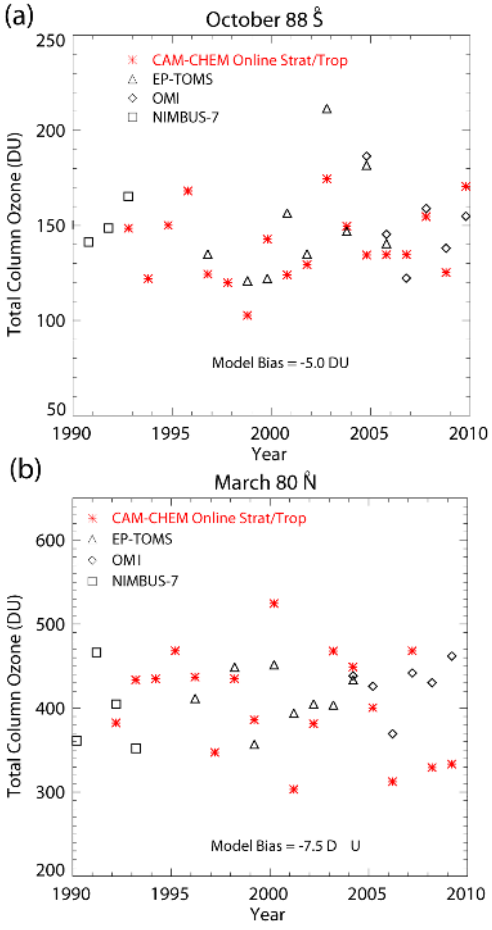

Fig. 14. **(a)** Timeseries of October total ozone column at 88° S. **(b)** Timeseries of March total ozone column at 80° N.

configuration to be slightly higher. Over the Eastern United States, all configurations are biased high, with the MERRA configuration leading to the highest biases (40–60 ppbv). It is unclear why ozone is biased high over those regions and is likely to be a combination of incorrect emissions, coarse resolution (Wild and Prather, 2006) and misrepresentation of physical processes (Lin et al. 2008). It is less likely to be meteorology-driven since online and specified dynamics behave similarly.

Over Europe (Fig. 8b), the model also tends to overestimate surface ozone. It is however clear that the online meteorology provides a much more biased ozone distribution (as can be seen in Fig. 6, region #5) than the specified dynamics. It is interesting to note that, in the model, the concentrations saturate at 80–90 ppbv, depending on the configuration, unlike the United States sites. Further analysis is necessary to understand this behavior.

7.2 Comparison with aircraft observations

As a standard benchmark evaluation, we have performed comparison with the aircraft observations in the Emmons et al. (2000) climatology (Fig. S4). In this section, we summarize the content of those figures (Fig. 9) by focusing on the regional averages for each campaign in the Emmons et al. (2000) climatology. We further concentrate our analysis on a specific range of altitude, 2–6 km in this case. This is chosen as to be representative of the free troposphere and be less directly influenced in possible emission shortcomings. Because we focus on the regional averages on the climatology, we include all simulations. In each case, we have used the monthly-averaged model results for the period 2006–2008, although the use of a longer period does not alter the conclusions (not shown).

As expected from the ozone analysis presented in Sect. 7.1, the GEOS5 simulation performs better than the other ones in its ozone distribution. Also, MERRA strongly overestimates ozone during the TOPSE (Northern Hemisphere high latitudes) campaigns, reinforcing the view of too strong mixing from the stratosphere.

Table 11. Slope of linear fit of annual mean modeled aerosols against IMPROVE data.

	Sulfate	EC	OC	Amm. Nit.
Online	0.99	0.37	0.36	0.93
GEOS5	2.12	0.41	0.39	0.91
MERRA	1.90	0.43	0.41	0.98

Nitrogen oxides (NO_x) tends to be highest in the online configuration (Fig. 9a), although all versions seem to exhibit similar biases; in particular, there is clear low NO_x bias in the case of TOPSE. Similarly, PAN and nitric acid (HNO_3) are consistently simulated across configurations. In most cases, the lowest CO distribution is associated with the GEOS5 simulation. This is discussed in more details in Sect. 7.3.

Except for the TOPSE campaign, the non-methane hydrocarbons (Fig. 9b) are quite well represented in the model over most of the campaigns, TOPSE being again the most biased with a strong underestimate in C_2H_6. There is a larger spread between configurations on methylhydroperoxide (CH_3OOH), where the online simulation is consistently the lowest and on hydrogen peroxide (H_2O_2) for which MERRA tends to be the lowest.

In order to identify the role of the wet removal parameterization (see Sect. 3.3), we perform the same analysis as above using the MERRA simulations (with the Horowitz and Neu and Prather schemes, see Table 6). Over the analysis regions (Fig. 10), we find little impact on ozone, NO_x or PAN. On the other hand, CO is consistently smaller (and therefore worse) when the Neu and Prather scheme is used. Furthermore, the nitric acid and hydrogen peroxide distributions over TOPSE are more accurately represented with the Horowitz scheme. However, in most cases, little difference can be found between those simulations.

7.3 Comparison with surface carbon monoxide

Surface mixing ratio of carbon monoxide represents one of longest records of tropospheric composition; for this comparison we use all years available from the National Oceanic and Atmospheric Administration data (available at ftp://ftp.cmdl.noaa.gov/ccg/co/flask/event/, Novelli and Masarie, 2010). Furthermore, because of its strong link to the hydroxyl radical OH, the overall concentration and seasonal cycle of CO (which in turn depends on emissions of CO and its precursors) is an important indicator of the representation of the tropospheric oxidative capacity (Lawrence et al., 2001). For that purpose, we compare the model results (in this case the online and MERRA simulations, in order to have a sufficiently long record) in terms of the latitudinal distribution of the annual mean and seasonal cycle (Fig. 11a and b, respectively).

Overall, the model accurately represents the latitudinal distribution of CO (strongly driven by gradients in emissions); it also represents the Southern Hemisphere annual mean, but underestimates the high-latitude Northern Hemisphere values, similar to the multi-model results in Shindell et al. (2006). The much higher than observed value close to the Equator is related to the Bukit Koto Tabang (West Sumatra) station, which being an elevated site (865 m) makes it challenging for coarse-grid models, especially for narrow islands. The bias could also be related to emission errors, although the Guam station (at 13° N) does not indicate a strong bias. Statistical evaluation is listed in Table 10. We find that, while the biases (annual mean and seasonal cycle) are lower in MERRA, the root-mean square difference is larger in that case. The higher correlation however indicates a better representation of the surface CO distribution in MERRA. Similarly, the seasonal cycle is quite well represented over all the latitudes, except in the Polar Northern Hemisphere.

This is further confirmed by the comparison to the retrieved CO 500 hPa concentrations by the Measurements of Pollution in The Troposphere (MOPITT v4, Deeter et al., 2010, Fig. 12). We find that all versions tend to overestimate the CO over Africa in December–February. During summer, the online version tends to reproduce the African maximum better.

The estimated CO tropospheric lifetime (with respect to OH loss, ozone <100 ppbv) is approximately 1.5 months in the MERRA and GEOS5 simulations and 1.75 in the online simulation, similar to the results from Horowitz et al. (2003) and Shindell et al. (2006). We have also compared (see Supplement, Fig. S5) our tropospheric OH distribution with the Spivakovsky et al. (2000) climatology using the Lawrence et al. (2001) diagnostic approach. In that case, we find that our OH distribution is in quite good agreement with that climatology. It is however smaller (20–30%) in the tropical mid-troposphere, especially in the Southern Hemisphere; it is also larger in the Northern mid-latitudes, except in the mid-troposphere. Based on this analysis, the closest OH distribution to Spivakosky's is provided by the GEOS5 simulation.

The tropospheric methane lifetime (reaction with OH only, computed as total burden divided by tropospheric loss, with the troposphere defined as the region with ozone <100 ppbv) ranges between 8.7 and 9.8 yr (Table 9), similar to Shindell et al. (2006) and Horowitz et al. (2003), but lower than MOZART-4 (10.5 yr, E2010, albeit computed slightly differently) and therefore consistent with the above analysis of OH. This is also consistent with a drier tropical troposphere in the online simulation (Fig. 4a) and higher isoprene emissions (Table 6).

7.4 Comparison with total ozone column

The availability of stratospheric chemistry in the online simulation warrants the comparison with the satellite observed total ozone column. In particular, we use here the gridded

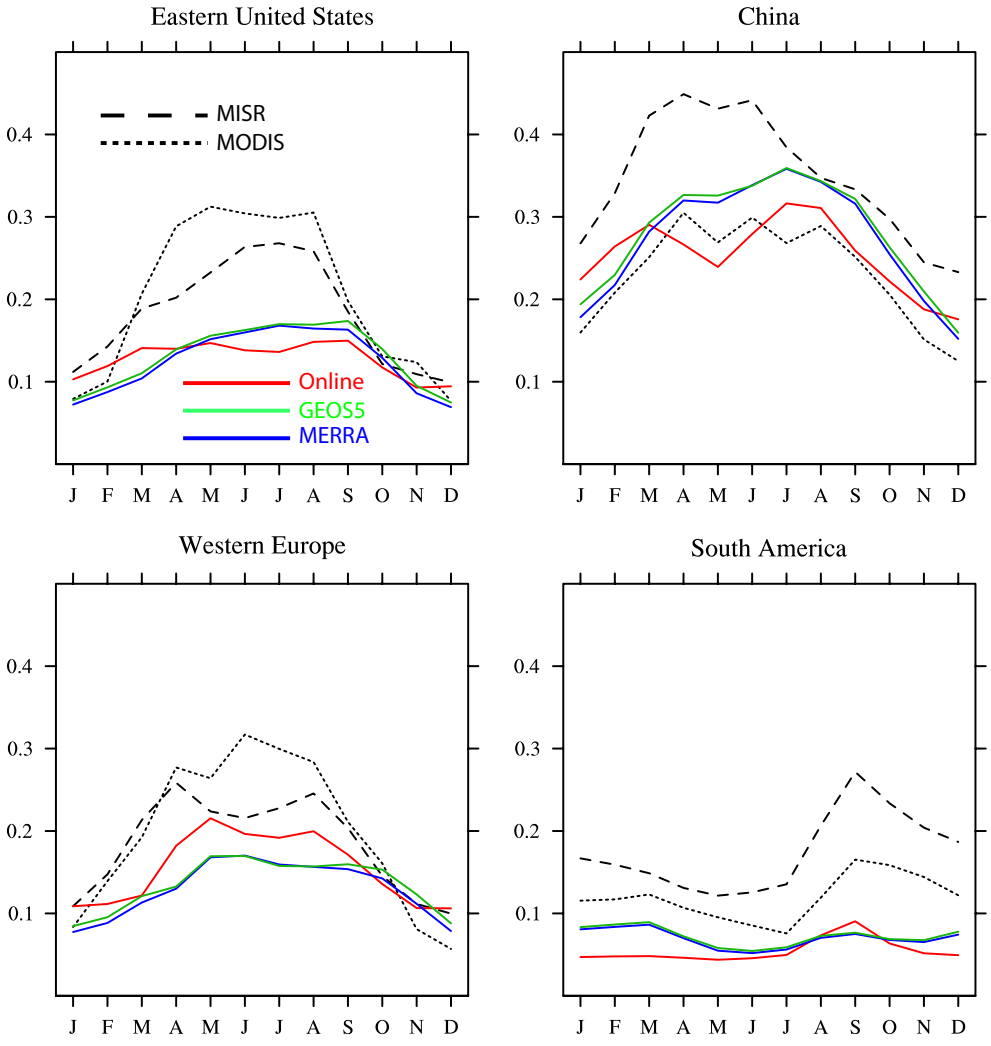

Fig. 15. Seasonal cycle of the aerosol optical depth from MODIS and MISR over specific regions.

EP-TOMS and OMI (both available at http://toms.gsfc.nasa.gov). The data are zonally- and monthly-averaged before comparison with the model field (Fig. 13). The overall features (latitudinal distribution and seasonal cycle, including the Antarctic ozone hole) and interannual variability are well reproduced. In particular, even though the model has a limited vertical extent and resolution in the stratosphere, the tropical ozone column is quite well reproduced.

To further compare with observed values, we focus (Fig. 14) on comparing the long-term variability in high-latitude spring ozone (March in the Northern Hemisphere and October in the Southern Hemisphere). Because the online model is only driven by the observed sea-surface temperatures, there is no expectation that a single-year in the model simulation will be directly comparable with observations; instead, only the mean and standard deviation are relevant in this case. Figure 14 shows that, unlike the version used in the CCMVal-2 simulations (Austin et al., 2010), this updated version has a good representation of the ozone hole (mean and interannual variability), with a limited underestimate (mean bias is −5.0 DU not considering the highly unusual 2002 conditions) of the mean October Antarctic ozone hole. Similarly the mean Northern Hemisphere March ozone distribution is slightly negatively biased (mean bias is −7.5 DU). These negative biases are likely due to the cold bias over the polar regions in the online configuration (see Fig. 4a). Note however that the model is not quite able to reproduce the Northern Hemisphere dynamical interannual variability due to its limited representation of the stratosphere (Morgenstern et al., 2010).

7.5 Comparison with aerosol observations

At the regional scale and over land, the modeled aerosol optical depth (Fig. 15) is generally lower than the satellite observations (from the Moderate Resolution Imaging Spectroradiometer and the Multi-angle Imaging SpectroRadiometer,

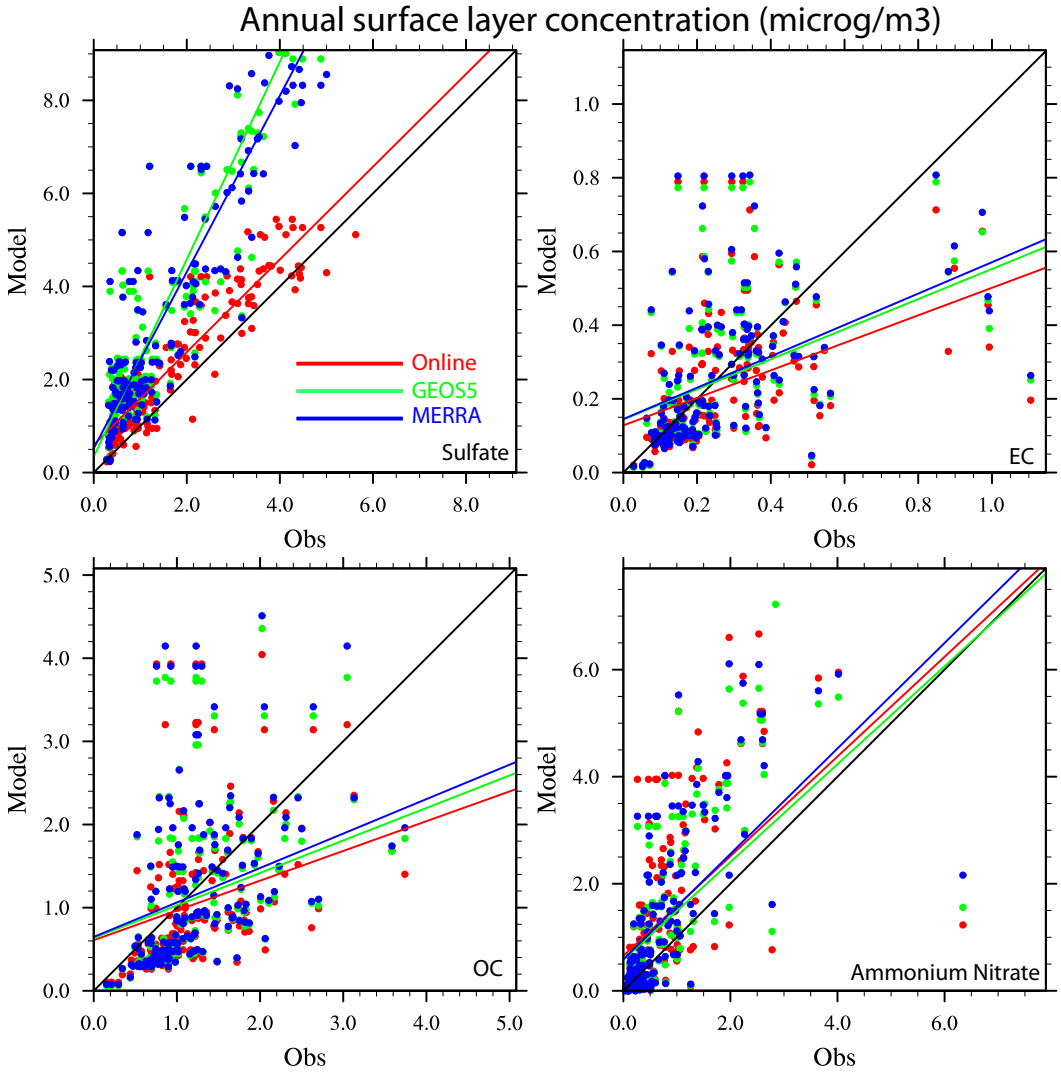

Fig. 16. Linear correlation between observed (IMPROVE sites, black line) and modeled (interpolated to observation sites) annual surface concentrations of aerosols (sulfate, top left; elemental carbon, top right, organic carbon, bottom left, ammonium nitrate, bottom right).

all years 2001–2010), except over China. As discussed in Lamarque et al. (2011b), none of these simulations include the impact of water uptake on black carbon optical properties, lowering the optical depth associated with this compound and partially explaining the negative bias, particularly over South America where biomass burning is the major source of optical depth. It is likely that the more important tropical precipitation in the online simulation significantly contributes to the underestimation in optical depth.

Owing to the availability of a large set of surface observations (time and speciation), we focus our analysis on the United States Interagency Monitoring of Protected Visual Environments (IMPROVE, Malm et al., 2004) dataset (available for download at http://vista.cira.colostate.edu/IMPROVE/Data/data.htm). We perform a comparison of sulfate, elemental carbon, organic carbon (including secondary organic aerosols, SOA) and ammonium nitrate.

We first present correlations (Fig. 16) between long-term mean (1998–2009) observations and model results (interpolated to the location of the observing stations); note that the IMPROVE sites are located in remote locations (such as National Parks) and are therefore representative of the rural environment, not urban. We find that, as discussed in Lamarque et al. (2011b), sulfate is quite well represented by the online configuration, however slightly positively biased. On the other hand, both elemental and organic carbon aerosols are underestimated (and with large scatter) in all configurations.

The linear fit parameters (Table 11) indicate that all configurations behave similarly, except in the case of sulfate. In that case, the slope for the online configuration is closest to the observations, while GEOS5 and MERRA overestimate the surface values by a factor of 2. It is possible that such disparity would be reduced if the SO_2 emissions were released

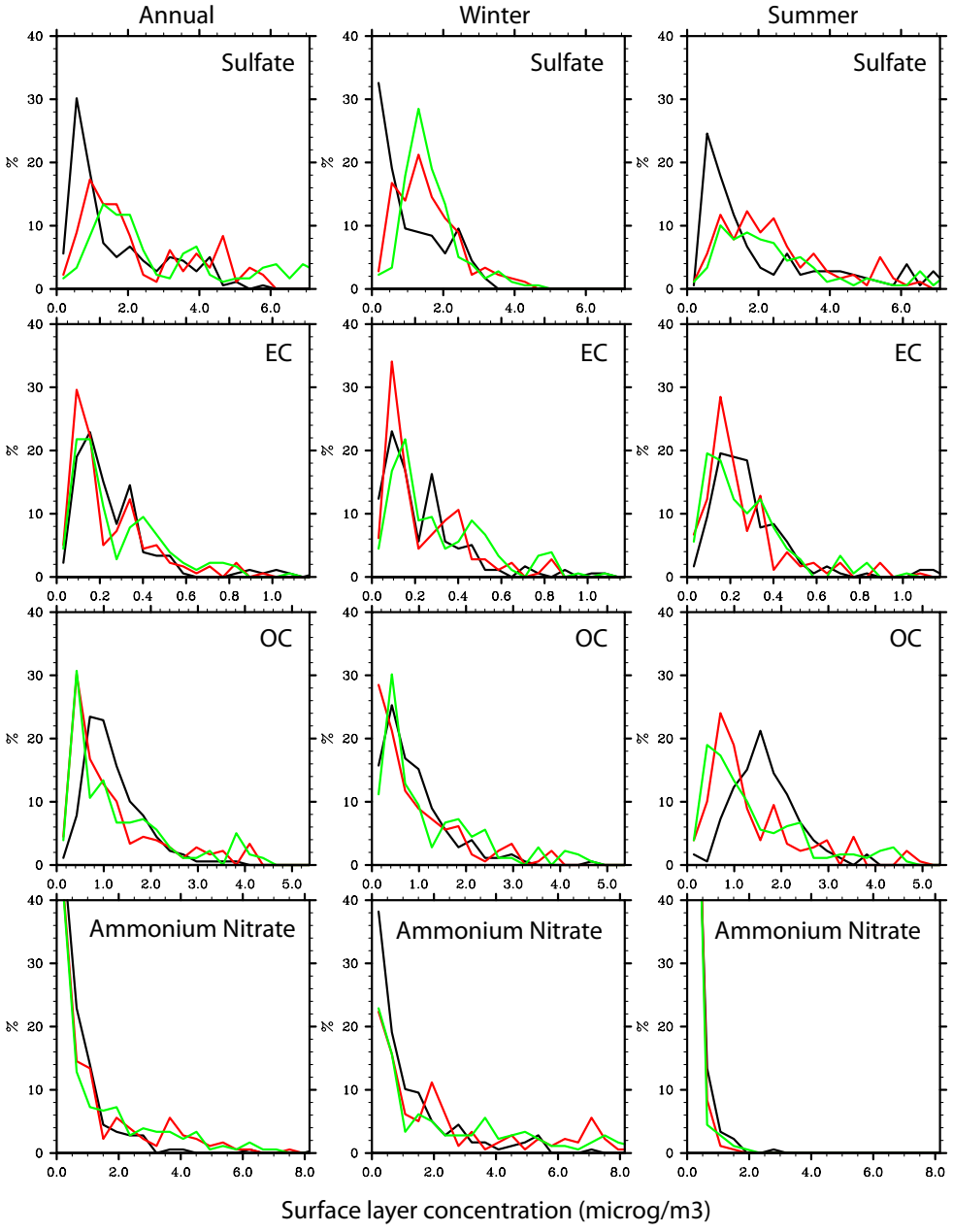

Fig. 17. Probability density function of observed (IMPROVE sites, black line) and modeled (interpolated to observation sites) aerosol surface concentration (sulfate, top row; elemental carbon, second row; organic carbon, third row; ammonium nitrate, bottom row). The simulation results shown here are for the online stratosphere-troposphere (red) and the GEOS5 simulation (green). Analysis is shown for annual (left column), winter (December-January-February, center column) and summer (June-July-August, right column).

at a specific height instead of the bottom model layer, which is much thinner in the specified dynamics set up (Fig. 3).

To further document the behavior of the bulk-aerosol scheme over the United States, we present in Fig. 17 the probability density function of the mean annual and seasonal (summer and winter) observed and modeled surface concentrations. Using this diagnostic, we find that the modeled sulfate cannot capture the lowest observed values and instead peaks at higher values and has a broader distribution; in addition, the annual mean seems to exhibit a longer tail in the distribution than the observations. Furthermore, the distribution function for elemental carbon is quite well reproduced, except for a higher tendency for small values. On the other hand it is clear that the model simulations of organic carbon cannot capture the mid-range values, especially in the summertime, most likely a representation of the lack of significant

SOA production with the current scheme (Lack et al., 2004). Somewhat surprisingly, owing to the inherent difficulties in representing ammonium nitrate in a model and to the fairly simple representation of its formation in the model, we find that ammonium nitrate is quite reasonable, with a slightly smaller proportion for the high concentrations (possibly due to the model coarse resolution) and higher proportion for the low concentrations.

8 Discussion and conclusions

Using a variety of diagnostics and evaluation datasets (including satellite, aircraft, surface measurements and surface data), we have demonstrated the capability of CAM-chem in reasonably representing tropospheric and stratospheric chemistry.

Based on the simulations discussed here, we have found that the CO and CH_4 lifetimes are in good agreement with previously published estimates; similarly, our OH distribution is in reasonable agreement with the Spivakovsky et al. (2000) climatology. However, our CO distribution in the high Northern latitudes is underestimated when compared to surface, aircraft and satellite observations, indicating an overestimate of the CO loss by OH or underestimate of its emissions or chemical production.

Ozone in the troposphere is simulated reasonably well, with some overestimation of ozone in the upper troposphere/lower stratosphere region in high northern latitudes in comparison to ozone sondes. Even though the model top is limited to 40 km, stratospheric composition is acceptable and the polar ozone depletion is reasonably well reproduced in the online configuration. All configurations of CAM-chem suffer from a significant overestimate of summertime surface ozone over the Eastern United States and Europe. On other hand, Western United States sites are quite accurately represented.

Aerosol optical depth tends to be underestimated over most regions when compared to satellite retrievals. Additional comparison over the United States indicates an overestimate of sulfate in the case of MERRA and GEOS5, and an underestimate of elemental and organic carbon in all configurations. Analysis of the seasonal (summer/winter) and annual probability density functions indicates strong similarities between model configurations.

Using a variety of statistical measures and especially Taylor diagrams, we have found that the CAM-chem configuration with GEOS5 meteorology provides the best representation of tropospheric chemistry. This is particularly clear for the 500 hPa (best bias and correlation) and 900 hPa (best bias) regional ozone distribution. The increased vertical resolution in GEOS5 and MERRA (56 levels instead of 26 for the online meteorology) might play a role in this better performance, although this hypothesis has not been explicitly tested. Based on the ozone budget analysis (and supported by ozone analysis in the high-latitudes), we have found that the MERRA meteorology leads to a stronger ozone flux from the stratosphere. This is likely associated with the different assimilation procedures used in MERRA than in GEOS5 (Rienecke et al., 2011).

When compared against regional climatologies from field campaigns, the inclusion of the Neu and Prather (2011) parameterization for wet removal of gas-phase species shows little impact on 2–6 km ozone. On the other hand, CO is consistently smaller (by 5–10 ppb). Consistent with this, the methane lifetime is slightly shorter with the Neu and Prather scheme. Nitric acid and hydrogen peroxide are increased over the high northern latitudes (TOPSE campaign). Overall, our analysis suggests only small differences from this new parameterization.

All necessary inputs (model code and datasets) to perform the simulations described here on a wide variety of computing platforms and compilers can be found at http://www.cesm.ucar.edu/models/cesm1.0/.

Supplementary material related to this article is available online at: http://www.geosci-model-dev.net/5/369/2012/gmd-5-369-2012-supplement.pdf.

Acknowledgements. We would like to acknowledge the help of M. Schultz and M. Val Martin with surface ozone measurements. P. G. H. was partially funded under the NSF award 0840825 and EPA Grant #: 834283. C. L. H. was partially supported by NSF award 0929282. D. K., J.-F. L. and F. V. were partially funded by the Department of Energy under the SciDAC program. We also acknowledge the science teams producing the data used for model evaluation, including the NOAA Earth System Research Laboratory Global Monitoring Division for surface CO and ozone sondes, and the World Ozone and Ultraviolet Radiation Data Centre (WOUDC) for ozonesondes. The CESM project is supported by the National Science Foundation and the Office of Science (BER) of the US Department of Energy. The National Center for Atmospheric Research is operated by the University Corporation for Atmospheric Research under sponsorship of the National Science Foundation.

Edited by: A. Stenke

References

Aghedo, A. M., Bowman, K. W., Worden, H. M., Kulawik, S. S., Shindell, D. T., Lamarque, J.-F., Faluvegi, G., Parrington, M., Jones, D. B. A., and Rast, S.: The vertical distribution of ozone instantaneous radiative forcing from satellite and chemistry climate models, J. Geophys. Res., 116, D01305, doi:10.1029/2010JD014243, 2011.

Andres, R. and Kasgnoc, A.: A time-averaged inventory of subaerial volcanic sulfur emissions, J. Geophys. Res., 103, 25251–25261, 1998.

Anenberg, S. C., West, J. J., Fiore, A. M., Jaffe, D. A., Prather, M. J., Bergmann, D., Cuvelier, K., Dentener, F. J., Duncan, B. N., Gauss, M., Hess, P., Jonson, J. E., Lupu, A., MacKenzie, I. A., Marmer, E., Park, R. J., Sanderson, M. G., Schultz, M., Shindell, D. T., Szopa, S., Vivanco, M. G., Wild, O., and Zang G.: Intercontinental impacts of ozone pollution on human mortality, Environ. Sci. Technol., 43, 6482–6487, 2009.

Austin, J., Struthers, H., Scinocca, J., Plummer, D., Akiyoshi, H., Baumgaertner, A. J. G., Bekki, S., Bodeker, G. E., Braesicke, P., Bruhl, C., Butchart, N., Chipperfield, M., Cugnet, D., Dameris, M., Dhomse, S., Frith, S., Garny, H., Gettelman, A., Hardiman, S., Jockel, P., Kinnison, D., Lamarque, J.-F., Marchand, M., Michou, M., Morgenstern, O., Nakamura, T., Nielsen, J. E., Pitari, G., Pyle, J., Shepherd, T. G., Shibata, K., Smale, D., Stolarski, R., Teyssedre, H., and Yamashita, Y.: Chemistry climate model simulations of the Antarctic ozone hole, J. Geophys. Res., 115, D00M11, doi:10.1029/2009JD013577, 2010.

Barth, M. C., Rasch, P. J., Kiehl, J. T., Benkovitz, C. M., and Schwartz, S. E.: Sulfur chemistry in the National Center for Atmospheric Research Community Climate Model: Description, evaluation, features, and sensitivity to aqueous chemistry, J. Geophys. Res., 105, 1387–1415, doi:10.1029/1999JD900773, 2000.

Bond, T., Streets, D. G., Yarber, K. F., Nelson, S. M., Woo, J.-H., and Klimont, Z.: A technology-based global inventory of black and organic carbon emissions from combustion, J. Geophys. Res., 109, D14203, doi:10.1029/2003JD003697, 2004.

Boville B. A., Rasch, P. J., Hack, J. J., and McCaa, J. R.: Representation of clouds and precipitation processes in the Community Atmosphere Model version 3 (CAM3), J. Climate, 19, 2184–2198, 2006.

Brasseur G. P., Hauglustaine,D. A., Walters, S., Rasch,P. J., Muller, J.-F. , Granier, C., and Tie, X. X.: MOZART, a global chemical transport model for ozone and related chemical tracers 1. Model description, J. Geophys. Res., 103, 28265–28289, 1998.

Butchart, N., Charlton-Perez, A. J., Cionni, I., Hardiman, S. C., Haynes, P. H., Kruger, K., Kushner, P. J., Newman, P. A., Osprey, S. M., Perlwitz, J., Sigmond, M., Wang, L., Akiyoshi, H., Austin, J., Bekki, S., Baumgaertner, A., Braesicke, P., Bruhl, C., Chipperfield, M., Dameris, M., Dhomse, S., Eyring, V., Garcia, R., Garny, H., Jockel, P., Lamarque, J.-F., Marchand, M., Michou, M., Morgenstern, O., Nakamura, T., Pawson, S., Plummer, D., Pyle, J., Rozanov, E., Scinocca, J., Shepherd, T. G., Shibata, K., Smale, D., Teyssedre, H., Tian, W., Waugh, D. and Yamashita, Y.: Multi-model climate and variability of the stratosphere, J. Geophys. Res., 116, D05102, doi:10.1029/2010JD014995, 2011.

Chen, J., Avise, J., Lamb, B., Salathé, E., Mass, C., Guenther, A., Wiedinmyer, C., Lamarque, J.-F., O'Neill, S., McKenzie, D., and Larkin, N.: The effects of global changes upon regional ozone pollution in the United States, Atmos. Chem. Phys., 9, 1125–1141, doi:10.5194/acp-9-1125-2009, 2009.

Collins W. D., Rasch, P. J., Boville, B. A., Hack, J. J., McCaa, J. R., Williamson, D. L., Briegleb, B., Bitz, C. M., Lin, S.-J., and Zhang, M.: The Community Climate System Model version 3 (CCSM3), J. Climate, 19, 2122–2143, 2006.

Collins, W. J., Bellouin, N., Doutriaux-Boucher, M., Gedney, N., Halloran, P., Hinton, T., Hughes, J., Jones, C. D., Joshi, M., Liddicoat, S., Martin, G., O'Connor, F., Rae, J., Senior, C., Sitch, S., Totterdell, I., Wiltshire, A., and Woodward, S.: Development and evaluation of an Earth-System model – HadGEM2, Geosci. Model Dev., 4, 1051–1075, doi:10.5194/gmd-4-1051-2011, 2011.

Considine, D. B., Douglass, A. R., Kinnison, D. E., Connell, P. S., and Rotman, D. A. : A polar stratospheric cloud parameterization for the three dimensional model of the global modeling initiative and its response to stratospheric aircraft emissions, J. Geophys. Res., 105, 3955–3975, 2000.

Cooke, W. F., Liousse, C., Cachier, H., and Feichter, J.: Construction of a 1x1 fossil fuel emission data set for carbonaceous aerosol and implementation and radiative impact in the ECHAM4 model, J. Geophys. Res., 104, 22137–22162, 1999.

DeCaria, A. J., Pickering, K. E., Stenchikov, G. L., and Ott, L. E.: Lightning-generated NOX and its impact on tropospheric ozone production: Athree-dimensional modeling study of a Stratosphere-Troposphere Experiment: Radiation, Aerosols and Ozone (STERAO-A) thunderstorm, J. Geophys. Res., 110, D14303, doi:10.1029/2004JD005556, 2006.

Deeter, M., Edwards, D. P., Gille, J. C., Emmons, L. K., Francis, G., Ho, S.-P., Mao, D., Masters, D., Worden, H., Yudin, V., and Drummond, J. R.: The MOPITT Version 4 CO product: Algorithm enhancements, selected results and bias drift, J. Geophys. Res., 115, D07306, doi:10.1029/2009JD013005, 2010.

Emmons, L. K., Hauglustaine, D. A., Müller, J.-F., Carroll, M. A., Brasseur, G. P., Brunner, D., Staehelin, J., Thouret, V., and Marenco, A.: Data composites of airborne observations of tropospheric ozone and its precursors, J. Geophys. Res., 105, 20497–20538, 2000.

Emmons, L. K., Walters, S., Hess, P. G., Lamarque, J.-F., Pfister, G. G., Fillmore, D., Granier, C., Guenther, A., Kinnison, D., Laepple, T., Orlando, J., Tie, X., Tyndall, G., Wiedinmyer, C., Baughcum, S. L., and Kloster, S.: Description and evaluation of the Model for Ozone and Related chemical Tracers, version 4 (MOZART-4), Geosci. Model Dev., 3, 43–67, doi:10.5194/gmd-3-43-2010, 2010.

Fiore, A. M., Dentener, F. J., Wild, O., Cuvelier, C., Schultz, M. G., Hess, P., Textor, C., Schulz, M., Doherty, R. M., Horowitz, I. A., MacKenzie, M. G., Sanderson, D. T. Shindell, D. S., Stevenson, S., Szopa, R., Van Dingenen, G., Zeng, C., Atherton, D., Bergmann, L. W., I. Bey, G., Carmichael, W. J., Collins, B. N., Duncan, G., Faluvegi, G., Folberth, M., Gauss, S., Gong, D., Hauglustaine, T., Holloway, I. S. A., Isaksen, D. J., Jacob, J. E., Jonson, J. W., Kaminski, T. J., Keating, A., Lupu, E., Marmer, V., Montanaro, R. J., Park, G., Pitari, K. J., Pringle, J. A., Pyle, S., Schroeder, M. G., Vivanco, P., Wind, G., Wojcik, S., Wu, and Zuber, A.: Multi-Model estimates of intercontinental source-receptor relationships for ozone pollution, J. Geophys. Res., 114, D04301, doi:10.1029/2008JD010816, 2009.

Forster, P. V., Ramaswamy, V., Artaxo, P., Berntsen, T., Betts, R., Fahey, D. W., Haywood, J., Lean, J., Lowe, D. C., Myhre, G., Nganga, J., Prinn, R., Raga, G., Schulz, M., and Van Dorland, R.: Changes in Atmospheric Constituents and in Radiative Forcing, in: Climate Change 2007: The Physical Science Basis, Contribution of Working Group I to the Fourth Assessment Report of the Intergovernmental Panel on Climate Change, edited by: Solomon, S., Qin, D., Manning, M., Chen, Z., Marquis, M., Averyt, K. B., Tignor, M., and Miller, H. L., Cambridge University Press, Cambridge, UK and New York, NY, USA, 2007.

Garcia, R. R., Marsh, D. R., Kinnison, D. E., Boville, B. A., and Sassi, F.: Simulation of secular trends in the mid-

dle atmosphere, 1950–2003, J. Geophys. Res., 112, D09301, doi:10.1029/2006JD007485, 2007.

Granier, C., Guenther, A., Lamarque, J., Mieville, A., Muller, J., Olivier, J., Orlando, J., Peters, J., Petron, G., Tyndall, G., and Wallens, S.: POET, a database of surface emissions ofozone precursors, available at: http://www.aero.jussieu.fr/projet/ACCENT/POET.php, (last access: August 2008), 2005.

Guenther, A., Hewitt, C. N., Erickson, D., Fall, R., Geron, C., Graedel, T., Harley, P., Klinger, L., Lerdau, M., McKay, W., Pierce, T., Scholes, B., Steinbrecher, R., Tallamraju, R., Taylor, J., and Zimmerman, P.: A global model of natural volatile organic compound emissions, J. Geophys. Res., 100, 8873–8892, 1995.

Guenther, A., Karl, T., Harley, P., Wiedinmyer, C., Palmer, P. I., and Geron, C.: Estimates of global terrestrial isoprene emissions using MEGAN (Model of Emissions of Gases and Aerosols from Nature), Atmos. Chem. Phys., 6, 3181–3210, doi:10.5194/acp-6-3181-2006, 2006.

Hack, J. J., Caron, J. M., Yeager, S. G., Oleson, K. W., Holland, M. M., Truesdale, J. E., and Rasch, P. J.: Simulation of the global hydrological cycle in the CCSM Community Atmosphere Model Version 3 (CAM3): Mean features, J. Climate, 19, 2199–2221, 2006.

Heald, C. L., Henze, D. K., Horowitz, L. W., Feddema, J., Lamarque, J.-F., Guenther, A., Hess, P. G., Vitt, F., Seinfeld, J. H., Goldstein, A. H., and Fung, I.: Predicted change in global secondary organic aerosol concentrations in response to future climate, emissions, and land-use change, J. Geophys. Res., 113, D05211, doi:10.1029/2007JD009092, 2008.

Holtslag, A. A. M. and Boville, B. A.: Local versus nonlocal boundary layer diffusion in a global climate model, J. Climate, 6, 1825–1841, 1993.

Horowitz, L. W., Walters, S., Mauzerall, D. L., Emmons, L. K., Rasch, P. J., Granier, C., Tie, X. X., Lamarque, J.-F., Schultz, M. G., Tyndall, G. S., Orlando, J. J., and Brasseur, G. P.: A global simulation of tropospheric ozone and related tracers: Description and evaluation of MOZART, version 2, J. Geophys. Res., 108, 4784, doi:10.1029/2002JD002853, 2003.

Hsu, J., Prather, M. J., and Wild, O.: Diagnosing the stratosphere-to-troposphere flux of ozone in a chemistry transport model, J. Geophys. Res., 110, D19305, doi:10.1029/2005JD006045, 2005.

Hudman, R. C., Jacob, D. J., Turquety, S., Leibensperger, E. M., Murray, L. T., Wu, S., Gilliland, A. B., Avery, M., Bertram, T. H., Brune, W., Cohen, R. C., Dibb, J. E., Flocke, F. M., Fried, A., Holloway, J., Neuman, J. A., Orville, R., Perring, A., Ren, X., Sachse, G. W., Singh, H. B., Swanson, A., and Wooldridge, P. J.: Surface and lightning sources of nitrogen oxides over the United States: Magnitudes, chemical evolution, and outflow, J. Geophys. Res., 112, D12S05, doi:10.1029/2006JD007912, 2007.

Jacob, D. J. and Winner, D. A.: Effect of Climate Change on Air Quality, Atmos. Environ., 43, 51–63, doi:10.1016/j.atmosenv.2008.09.05, 2009.

Jakob, C. and Klein, S. A.: A parametrization of cloud and precipitation overlap effects for use in General Circulation Models, Q. J. Roy. Meteorol. Soc., 126, 2525–2544, 2000.

Jonson, J. E., Stohl, A., Fiore, A. M., Hess, P., Szopa, S., Wild, O., Zeng, G., Dentener, F. J., Lupu, A., Schultz, M. G., Duncan, B. N., Sudo, K., Wind, P., Schulz, M., Marmer, E., Cuvelier, C., Keating, T., Zuber, A., Valdebenito, A., Dorokhov, V., De Backer, H., Davies, J., Chen, G. H., Johnson, B., Tarasick, D. W., Stübi, R., Newchurch, M. J., von der Gathen, P., Steinbrecht, W., and Claude, H.: A multi-model analysis of vertical ozone profiles, Atmos. Chem. Phys., 10, 5759–5783, doi:10.5194/acp-10-5759-2010, 2010.

Kärcher, B. and Voigt, C.: Formation of nitric acid/water ice particles in cirrus clouds, Geophys. Res. Lett., 33, L08806, doi:10.1029/2006GL025927, 2006.

Kinnison, D. E., Brasseur, G. P., Walters, S., Garcia, R. R., Marsh, D. A., Sassi, F., Boville, B. A., Harvey, L., Randall, C., Emmons, L., Lamarque, J.-F., Hess, P., Orlando, J., Tyndall, G., Tie, X. X., Randel, W., Pan, L., Gettelman, A., Granier, C., Diehl, T., Niemeier, U., and Simmons, A. J.: Sensitivity of chemical tracers to meteorological parameters in the MOZART-3 chemical transport model, J. Geophys. Res., 112, D20302, doi:10.1029/2006JD007879, 2007.

Kloster, S., Feichter, J., Maier-Reimer, E., Six, K. D., Stier, P., and Wetzel, P.: DMS cycle in the marine ocean-atmosphere system – a global model study, Biogeosciences, 3, 29–51, doi:10.5194/bg-3-29-2006, 2006.

Lack, D. A., Tie, X. X., Bofinger, N. D., Wiegand, A. N., and Madronich, S.: Seasonal variability of secondary organic aerosol: A global modeling study, J. Geophys. Res., 109, D03202, doi:10.1029/2003JD003418, 2004.

Lamarque, J.-F. and Solomon, S.: Impact of Changes in Climate and Halocarbons on Recent Lower Stratosphere Ozone and Temperature Trends, J. Climate, 23, 2599–2611, 2010.

Lamarque, J.-F., Kiehl, J. T., Hess, P. G., Collins, W. D., Emmons, L. K., Ginoux, P., Luo, C., and Tie, X. X.: Response of a coupled chemistry-climate model to changes in aerosol emissions: Global impact on the hydrological cycle and the tropospheric burdens of OH, ozone and NOx, Geophys. Res. Lett., 32, L16809, doi:10.1029/2005GL023419, 2005.

Lamarque, J.-F., Kinnison, D. E., Hess, P. G., and Vitt, F.: Simulated lower stratospheric trends between 1970 and 2005: identifying the role of climate and composition changes, J. Geophys. Res., 113, D12301, doi:10.1029/2007JD009277, 2008.

Lamarque, J.-F., Bond, T. C., Eyring, V., Granier, C., Heil, A., Klimont, Z., Lee, D., Liousse, C., Mieville, A., Owen, B., Schultz, M. G., Shindell, D., Smith, S. J., Stehfest, E., Van Aardenne, J., Cooper, O. R., Kainuma, M., Mahowald, N., McConnell, J. R., Naik, V., Riahi, K., and van Vuuren, D. P.: Historical (1850–2000) gridded anthropogenic and biomass burning emissions of reactive gases and aerosols: methodology and application, Atmos. Chem. Phys., 10, 7017–7039, doi:10.5194/acp-10-7017-2010, 2010.

Lamarque, J.-F., McConnell, J. R., Shindell, D. T., Orlando, J. J., and Tyndall, G. S.: Understanding the drivers for the 20th century change of hydrogen peroxide in Antarctic ice-cores, Geophys. Res. Lett., 38, L04810, doi:10.1029/2010GL045992, 2011a.

Lamarque, J.-F., Kyle, G. P., Meinshausen, M., Riahi, K., Smith, S. J., van Vuuren, D. P., Conley, A., and Vitt, F.: Global and regional evolution of short-lived radiatively-active gases and aerosols in the Representative Concentration Pathways, Climatic Change, 109, 191–212, 2011b.

Lauritzen, P. H., Ullrich, P. A., and Nair, R. D.: Atmospheric transport schemes: Desirable properties and a semi-Lagrangian view on finite-volume discretizations, in Numerical Techniques

for Global Atmospheric Models, Lect. Notes Comp. Sci., 80, Springer, Berlin, 2011.

Lawrence, M. G., Jöckel, P., and von Kuhlmann, R.: What does the global mean OH concentration tell us?, Atmos. Chem. Phys., 1, 37–49, doi:10.5194/acp-1-37-2001, 2001.

Lawrence, P. J. and Chase, T. N.: Representing a new MODIS consistent land surface in the Community Land Model (CLM 3.0), J. Geophys. Res., 112, G01023, doi:10.1029/2006JG000168, 2007.

Levis, S., Wiedinmyer, C., Guenther, A., and Bonan, G.: Coupling Biogenic VOC Emissions to the Community Land Model: Effects of Land Use Change on BVOC emissions, J. Geophys. Res., 108, 4659, doi:10.1029/2002JD003203, 2003.

Liao, H., Adams, P. J., Chung, S. H., Seinfeld, J. H., Mickley, L. J., and Jacob, D. J.: Interactions between tropospheric chemistry and aerosols in a unified general circulation model, J. Geophys. Res., 108, 4001, doi:10.1029/2001JD001260, 2003.

Lin, J.-T., Youn, D., Liang, X.-Z., and Wuebbles, D. J.: Global model simulation of summertime US ozone diurnal cycle and its sensitivity to PBL mixing, spatial resolution, and emissions, Atmos. Environ., 42, 8470–8483, doi:10.1016/j.atmosenv.2008.08.012, 2008.

Logan, J. A.: Trends in the vertical distribution of ozone: An analysis of ozonesonde data, J. Geophys. Res., 99, 25553–25585, 1994.

Lowe, D. and Mackenzie, R.: Review of polar stratospheric cloud microphysics and chemistry, J. Atmos Solar-Terr. Phys., 70, 13–40, 2008.

Madronich, S.: Photodissociation in the atmosphere 1. Actinic flux and the effects of ground reflections and clouds, J. Geophys. Res., 92, 9740–9752, 1987.

Mahowald, N., Lamarque, J.-F., Tie, X. X., and Wolff, E: Sea-salt aerosol response to climate change: Last Glacial Maximum, preindustrial, and doubled carbon dioxide climates, J. Geophys. Res. 111, D05303, doi:10.1029/2005JD006459, 2006a.

Mahowald, N. M., Muhs, D. R., Levis, S., Rasch, P. J., Yoshioka, M., Zender, C. S., and Luo, C.: Change in atmospheric mineral aerosols in response to climate: Last glacial period, preindustrial, modern, and doubled carbon dioxide climates, J. Geophys. Res., 111, D10202, doi:10210.11029/12005JD006653, 2006b.

Malm, W. C., Schichtel, B. A., Pitchford, M. L., Ashbaugh L. L., and Eldred, R. A.: Spatial and monthly trends in speciated fine particle concentration in the United States, J. Geophys. Res., 109, D03306, doi:10.1029/2003JD003739, 2004.

McLinden, C., Olsen, S., Hannegan, B., Wild, O., and Prather, M.: Stratospheric ozone in 3-D models: A simple chemistry and the cross-tropopause flux, J. Geophys. Res., 105, 14653–14665, 2000.

Meinshausen, M., Smith, S. J., Calvin, K., Daniel, J. S., Kainuma, M. L. T., Lamarque, J.-F., Matsumoto, K., Montzka, S., Raper, S., Riahi, K., Thomson, A., Velders, G. J. M., and van Vuuren, D. P.: The RCP Greenhouse Gas Concentrations and their Extensions from 1765 to 2300, Climatic Change, 109, 213–241, 2011.

Metzger, S., Dentener, F., Pandis, S., and Lelieveld, J.: Gas/aerosol partitioning: 1. A computationally efficient model, J. Geophys. Res., 107, 4312, doi:10.1029/2001JD001102, 2002.

Morgenstern, O., Akiyoshi, H. H., Bekki, S., Braesicke, P., Chipperfield, M., Gettelman, A., Hardiman, S., Lamarque, J.-F., Michou, M., Pawson, S., Rozanov, E., Scinocca, J., Shibata, K., and Smale, D.: Anthropogenic forcing of the Northern Annular Mode in CCMVal-2 models, J. Geophys. Res., 115, D00M03, doi:10.1029/2009JD013347, 2010.

Neale, R. B., Richter, J., and Jochum, M.: The impact of convection on ENSO: From a delayed oscillator to a series of events, J. Climate, 21, 5904–5924, 2008.

Neale, R. B., Richter, J., Park, S., Lauritzen, P. H., Vavrus, S. J., Rasch, P. J., and Zhang, M.: The Mean Climate of the Community Atmosphere Model (CAM4) in Forced SST and Fully Coupled Experiments, J. Climate, submitted, 2011.

Neu, J. L. and Prather, M. J.: Toward a more physical representation of precipitation scavenging in global chemistry models: cloud overlap and ice physics and their impact on tropospheric ozone, Atmos. Chem. Phys. Discuss., 11, 24413–24466, doi:10.5194/acpd-11-24413-2011, 2011.

Novelli, P. C. and Masarie, K. A.: Atmospheric Carbon Monoxide Dry Air Mole Fractions from the NOAA ESRL Carbon Cycle Cooperative Global Air Sampling Network, 1988–2009, Version: 2011-10-14, available at: ftp://ftp.cmdl.noaa.gov/ccg/co/flask/event/ (last access: April 2011), 2010.

Ohara, T., Akimoto, H., Kurokawa, J., Horii, N., Yamaji, K., Yan, X., and Hayasaka, T.: An Asian emission inventory of anthropogenic emission sources for the period 1980–2020, Atmos. Chem. Phys., 7, 4419–4444, doi:10.5194/acp-7-4419-2007, 2007.

Oleson, K. W., Lawrence, D. M., Bonan, G. B., Flanner, M. G., Kluzek, E., Lawrence, P. J., Levis, S., Swenson, S. C., Thornton, P. E., Dai, A., Decker, M., Dickinson, R., Feddema, J., Heald, C. L., Hoffman, F., Lamarque, J.-F., Mahowald, N., Niu, G.-Y., Qian, T., Randerson, J., Running, S., Sakaguchi, K., Slater, A., Stockli, R., Wang, A., Yang, Z.-L., and Zeng, X.: Technical description of version 4.0 of the Community Land Model (CLM), NCAR Technical Note NCAR/TN-478+STR, 257 pp., 2010.

Pfister, G., Hess, P. G., Emmons, L. K., Rasch, P. J., and Vitt, F. M.: Impact of the Summer 2004 Alaska Fires on TOA Clear-Sky Radiation Fluxes, J. Geophys. Res., 113, D02204, doi:10.1029/2007JD008797, 2008.

Prather, M. J.: Tropospheric O_3 from photolysis of O_2, Geophys. Res. Lett., 36, L03811, doi:10.1029/2008GL036851, 2009.

Price, C. and Rind, D.: A simple lightning parameterization for calculating global lightning distributions, J. Geophys. Res., 97, 9919–9933, doi:10.1029/92JD00719, 1992.

Price, C., Penner, J., and Prather, M.: NO_x from lightning 1, Global distribution based on lightning physics, J. Geophys. Res., 102, 5929–5941, 1997.

Randerson, J., Liu, H., Flanner, M. G., Chambers, S. D., Jin, Y., Hess, P. G., Pfister, G., Mack, M. C., Treseder, K. K., Welp, L. R., Chapin, F. S., Harden, J. W., Goulden, M. L., Lyons, E., Neff, J. C., Schuur, E. A. G., and Zender, C. S.: The Impact of Boreal Forest Fires on Climate Warming, Science, 314, 1130–1132, doi:10.1126/science.1132075, 2006.

Rasch, P. J., Mahowald, N. M., and Eaton, B. E.: Representations of transport, convection, and the hydrologic cycle in chemical transport models: Implications for the modeling of short-lived and soluble species, J. Geophys. Res., 102, 28127–28138, 1997.

Rasch, P. J., Coleman, D. B., Mahowald, N., Williamson, D. L., Lin, S.-J., Boville, B. A., and Hess, P.: Characteristics of atmospheric transport using three numerical formulations for atmospheric dynamics in a single GCM framework, J. Climate, 19, 2243–2266, 2006.

Richter, J. H. and Rasch, P. J.: Effects of Convective Momentum Transport on the Atmospheric Circulation in the Community Atmosphere Model, Version 3, J. Climate, 21, 1487–1499. doi:10.1175/2007JCLI1789.1, 2007.

Ridley, B., Pickering, K., and Dye, J. : Comments on the parameterization of lightning-produced NO in global chemistry-transport models, Atmos. Environ., 39, 6184–6187, 2005.

Rienecker, M. M., Suarez, M. J., Gelaro, R., Todling, R., Bacmeister, J., Liu, E., Bosilovich, M. G., Schubert, S. D., Takacs, L., Kim, G.-K., Bloom, S., Chen, J., Collins, D., Conaty, A., da Silva, A., Gu, W., Joiner, J., Koster, R. D., Lucchesi, R., Molod, A., Owens, T., Pawson, S., Pegion, P., Redder, C. R., Reichle, R., Robertson, F. R., Ruddick, A. G., Sienkiewicz, M., and Woollen, J.: MERRA: NASA's Modern-Era Retrospective Analysis for Research and Application, J. Climate, 24, 3624–3648. doi:10.1175/JCLI-D-11-00015.1, 2011.

Rotman, D., Atherton, C. S., Bergmann, D. J., Cameron-Smith, P. J., Chuang, C. C., Connell, P. S., Dignon, J. E., Franz, A., Grant, K. E., Kinnison, D. E., Molenkamp, C. R., Proctor, D. D., and Tannahill, J. R.: IMPACT, the LLNL 3-D global atmospheric chemical transport model for the combined troposphere and stratosphere: Model description and analysis of ozone and other trace gases, J. Geophys. Res., 109, D04303, doi:10.1029/2002JD003155, 2004.

Rotstayn, L. D. and Lohmann, U.: Tropical rainfall trends and the indirect aerosol effect, J. Climate, 15, 2103–2116, 2002.

Sander, S. P., Friedl, R. R., Golden, D. M., Kurylo, M. J., Moortgat, G. K., Wine, P. H., Ravishankara, A. R., Kolb, C. E., Molina, M. J., Finlayson-Pitts, B. J., Huie, R. E., and Orkin, V.: Chemical Kinetics and Photochemical Data for Use in Atmospheric Studies – Evaluation Number 15, JPL Publication 06-2, 2006.

Sanderson, M., Collins, W., Derwent, R., and Johnson, C.: Simulation of global hydrogen levels using a Lagrangian three-dimensional model, J. Atmos. Chem., 46, 15–28, 2003.

Sanderson, M. G. Dentener, F. J., Fiore, A. M., Cuvelier, C., Keating, T. J., Zuber, A., Atherton, C. S., Bergmann, D. J., Diehl, T., Doherty, R. M., Duncan, B. N., Hess, P., Horowitz, L. W., Jacob, D. J., Jonson, J.-E., Kaminski, J. W., Lupu, A., MacKenzie, I. A., Mancini, E., Marmer, E., Park, R., Pitari, G., Prather, M. J., Pringle, K. J., Schroeder, S., Schultz, M. G., Shindell, D. T., Szopa, S., Wild, O., and Wind, P.: A multi-model source-receptor study of the hemispheric transport and deposition of oxidised nitrogen. Geophys. Res. Lett., 35, L17815, doi:10.1029/2008GL035389, 2008.

Shindell, D. T., Faluvegi, G., Stevenson, D. S., Krol, M. C., Emmons, L. K., Lamarque, J. F., Petron, G., Dentener, F. J., Ellingson, K., Schultz, M. G., Wild, O., Amann, M., Atherton, C. S., Bergmann, D. J., Bey, I., Butler, T., Cofala, J., Collins, W. J., Derwent, R. G., Doherty, R. M., Drevet, J., Eskes, H. J., Fiore, A. M., Gauss, M., Hauglustaine, D. A., Horowitz, L. W., Isaksen, I. S. A., Lawrence, M. G., Montanaro, V., Muller, J. F., Pitari, G., Prather, M. J., Pyle, J. A., Rast, S., Rodriguez, J. M., Sanderson, M. G., Savage, N. H., Strahan, S. E., Sudo, K., Szopa, S., Unger, N., van Noije, T. P. C., and Zen, G.: Multi-model simulations of carbon monoxide: Comparison with observations and projected near-future changes, J. Geophys. Res., 111, D19306, doi:10.1029/2006JD007100, 2006.

Shindell, D. T., Chin, M., Dentener, F., Doherty, R. M., Faluvegi, G., Fiore, A. M., Hess, P., Koch, D. M., MacKenzie, I. A., Sanderson, M. G., Schultz, M. G., Schulz, M., Stevenson, D. S., Teich, H., Textor, C., Wild, O., Bergmann, D. J., Bey, I., Bian, H., Cuvelier, C., Duncan, B. N., Folberth, G., Horowitz, L. W., Jonson, J., Kaminski, J. W., Marmer, E., Park, R., Pringle, K. J., Schroeder, S., Szopa, S., Takemura, T., Zeng, G., Keating, T. J., and Zuber, A.: A multi-model assessment of pollution transport to the Arctic, Atmos. Chem. Phys., 8, 5353–5372, doi:10.5194/acp-8-5353-2008, 2008.

SPARC CCMVal: Report on the Evaluation of Chemistry-Climate Models, edited by: Eyring, V., Shepherd, T. G., and Waugh, D. W., SPARC Repot No. 4, WCRP-X, WMO/TD-No. X, http://www.atmosp.physics.utoronto.ca/SPARC, 2010.

Sparks, J. P., Roberts, J. M., and Monson, R. K.: The uptake of gaseous organic nitrogen by leaves: A significant global nitrogen transfer process, Geophys. Res. Lett., 30, 2189, doi:10.1029/2003GL018578, 2003.

Spivakovsky, C. M., Logan, J. A., Montzka, S. A., Balkanski, Y. J., Foreman-Fowler, M., Jones, D. B. A., Horowitz, L. W., Fusco, A. C., Brenninkmeijer, C. A. M., Prather, M. J., Wofsy, S. C., and McElroy, M. B.: Three-dimensional climatological distribution of tropospheric OH: Update and evaluation, J. Geophys. Res., 105, 8931–8980, 2000.

Stevenson, D. S., Dentener, F. J., Schultz, M. G., Ellingsen, K., van Noije, T. P. C., Wild, O., Zeng, G., Amann, M., Atherton, C. S., Bell, N., Bergmann, D. J., Bey, I., Butler, T., Cofala, J., Collins, W. J., Derwent, R. G., Doherty, R. M., Drevet, J., Eskes, H. J., Fiore, A. M., Gauss, M., Hauglustaine, D. A., Horowitz, L. W., Isaksen, I. S. A., Krol, M. C., Lamarque, J.-F., Lawrence, M. G., Montanaro, V., Muller, J.-F., Pitari, G., Prather, M. J., Pyle, J. A., Rast, S., Rodriguez, J. M., Sanderson, M. G., Savage, N. H., Shindell, D. T., Strahan, S. E., Sudo, K., and Szopa, S.: Multi-model ensemble simulations of present-day andnear-future tropospheric ozone, J. Geophys. Res., 111, D08301, doi:10.1029/2005JD006338, 2005.

Tilmes, S., Lamarque, J.-F., Emmons, L. K., Conley, A., Schultz, M. G., Saunois, M., Thouret, V., Thompson, A. M., Oltmans, S. J., Johnson, B., and Tarasick, D.: Ozonesonde climatology between 1995 and 2009: description, evaluation and applications, Atmos. Chem. Phys. Discuss., 11, 28747–28796, doi:10.5194/acpd-11-28747-2011, 2011.

Tie, X., Brasseur, G., Emmons, L., Horowitz, L., and Kinnison, D.: Effects of aerosols on tropospheric oxidants: A global model study, J. Geophys. Res., 106, 22931–22964, 2001.

Tie, X., Madronich, S., Walters, S., Edwards, D. P., Ginoux, P., Mahowald, N., Zhang, R., Lou, C., and Brasseur, G.: Assessment of the global impact of aerosols on tropospheric oxidants, J. Geophys. Res., 110, D03204, doi:10.1029/2004JD005359, 2005.

Turnipseed, A., Huey, G., Nemitz, E., Stickel, R., Higgs, J., Tanner, D. and Slusher, D., Sparks, J., Flocke, F., and Guenther, A.: Eddy covariance fluxes of peroxyacyl nitrates (PANs) and NO_y to a coniferous forest, J. Geophys. Res., 111, D09304, doi:10.1029/2005JD006631, 2006.

van der Werf, G. R., Randerson, J. T., Giglio, L., Collatz, G. J., Kasibhatla, P. S., and Arellano Jr., A. F.: Interannual variability in global biomass burning emissions from 1997 to 2004, Atmos. Chem. Phys., 6, 3423–3441, doi:10.5194/acp-6-3423-2006, 2006.

Walcek, C. J., Brost, R. A., Chang, J. S., and Wesely, M. L.: SO_2, sulfate and HNO_3 deposition velocities computed using regional

landuse and meteorological data, Atmos. Environ., 20, 946–964, 1986.

Walmsley, J. L. and Wesely, M. L.: Modification of coded parameterizations of surface resistances to gaseous dry deposition, Atmos. Environ., 30, 1181–1188, 1996.

Wesely, M. L.: Parameterizations for surface resistance to gaseous dry deposition in regional-scale numerical models, Atmos. Environ., 23, 1293–1304, 1989.

Wesely, M. L. and Hicks, B. B.: A review of the current status of knowledge on dry deposition, Atmos. Environ., 34, 2261–2282, 2000.

Wiedinmyer, C., Akagi, S. K., Yokelson, R. J., Emmons, L. K., Al-Saadi, J. A., Orlando, J. J., and Soja, A. J.: The Fire INventory from NCAR (FINN): a high resolution global model to estimate the emissions from open burning, Geosci. Model Dev., 4, 625–641, doi:10.5194/gmd-4-625-2011, 2011.

Wild, O. and Prather, M. J.: Global tropospheric ozone modelling: Quantifying errors due to grid resolution, J. Geophys. Res., 111, D11305, doi:10.1029/2005JD006605, 2006.

Yonemura, S., Kawashima, S., and Tsuruta, H.: Carbon monoxide, hydrogen, and methane uptake by soils in a temperate arable field and a forest, J. Geophys. Res., 105, 14347–14362, 2000.

Zhang, G. J. and McFarlane, N. A.: Sensitivity of climate simulations to the parameterization of cumulus convection in the Canadian Climate Centre general circulation model, Atmos. Ocean, 33, 407–446, 1995.